

AD-A248 616

E200950



PL-TR-92-2005

2

NORSAR BASIC SEISMOLOGICAL RESEARCH

Editor:

Svein Mykkeltveit

NTNF/NORSAR  
Post Box 51  
N-2007 Kjeller, NORWAY

29 November 1991

Scientific Report No. 11



APPROVED FOR PUBLIC RELEASE; DISTRIBUTION UNLIMITED



PHILLIPS LABORATORY  
AIR FORCE SYSTEMS COMMAND  
HANSCOM AIR FORCE BASE, MASSACHUSETTS 01731-5000

92 3 11 022

92-06471




**Best  
Available  
Copy**

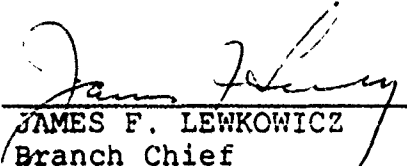
SPONSORED BY  
Defense Advanced Research Projects Agency  
Nuclear Monitoring Research Office  
ARPA ORDER NO. 5307

MONITORED BY  
Phillips Laboratory  
Contract F19628-89-C-0038

The views and conclusions contained in this document are those of the authors and should not be interpreted as representing the official policies, either expressed or implied, of the Defense Advanced Research Projects Agency or the U.S. Government.

This technical report has been reviewed and is approved for publication.

  
JAMES F. LEWKOWICZ  
Contract Manager  
Solid Earth Geophysics Branch  
Earth Sciences Division

  
JAMES F. LEWKOWICZ  
Branch Chief  
Solid Earth Geophysics Branch  
Earth Sciences Division

  
DONALD H. ECKHARDT, Director  
Earth Sciences Division

This report has been reviewed by the ESD Public Affairs Office (PA) and is releasable to the National Technical Information Service (NTIS).

Qualified requestors may obtain additional copies from the Defense Technical Information Center. All others should apply to the National Technical Information Service.

If your address has changed, or if you wish to be removed from the mailing list, or if the addressee is no longer employed by your organization, please notify PL/IMA, Hanscom AFB, MA 01731-5000. This will assist us in maintaining a current mailing list.

Do not return copies of this report unless contractual obligations or notices on a specific document requires that it be returned.

REPORT DOCUMENTATION PAGE			Form Approved OMB No. 0704-0188	
<small>Public reporting burden for this collection of information is estimated to average 1 hour per response, including the time for reviewing instructions, searching existing data sources, gathering and maintaining the data needed, and completing and reviewing the collection of information. Send comments regarding this burden estimate or any other aspect of this collection of information, including suggestions for reducing this burden, to Washington Headquarters Services, Directorate for Information Operations and Reports, 1215 Jefferson Davis Highway, Suite 1204, Arlington, VA 22202-4302, and to the Office of Management and Budget, Paperwork Reduction Project (0704-0188), Washington, DC 20503.</small>				
1. AGENCY USE ONLY (Leave blank)		2. REPORT DATE 29 November 1991		3. REPORT TYPE AND DATES COVERED Scientific Report No. 11
4. TITLE AND SUBTITLE NORSAR Basic Seismological Research			5. FUNDING NUMBERS PE 62714E PR 9A10 TA DA WU BH Contract F49620-89-C-0038	
6. AUTHOR(S) Editor:  Svein Mykkeltveit				
7. PERFORMING ORGANIZATION NAME(S) AND ADDRESS(ES) NTNF/NORSAR Post Box 51 N-2007 Kjeller, NORWAY			8. PERFORMING ORGANIZATION REPORT NUMBER	
9. SPONSORING/MONITORING AGENCY NAME(S) AND ADDRESS(ES) Phillips Laboratory Hanscom AFB, Massachusetts 01731-5000  Contract Manager: James Lewkowicz/GPEH			10. SPONSORING/MONITORING AGENCY REPORT NUMBER  PL-TR-92-2005	
11. SUPPLEMENTARY NOTES				
12a. DISTRIBUTION/AVAILABILITY STATEMENT  APPROVED FOR PUBLIC RELEASE; DISTRIBUTION UNLIMITED			12b. DISTRIBUTION CODE	
13. ABSTRACT (Maximum 200 words) This annual report describes the work accomplished under contract F49620-89-C-0038 during the period 1 October 1990-30 September 1991. The report contains four separate contributions (paragraphs 2.1 through 2.4), and in addition abstracts of the investigations submitted as quarterly technical reports during FY91 (paragraph 2.5). The inversion of NORSAR travel time data constituted one of the first examples of seismic tomography. It is now becoming apparent that these data are influenced by wave diffraction effects, and hence that ordinary (ray based) tomography may be inadequate. In paragraph 2.1 we apply a newly developed tomographic method that takes diffraction effects into account. Data from the NORSAR array in its original form (22 subarrays; aperture 100 km) have been used and results are compared with those of the ray-based inversion experiments undertaken around 15 years ago. To facilitate comparison with earlier results, we inverted for velocity structure in the same box-like structure as was used in the previous investigations. As we do not know the true structure beneath NORSAR, we cannot determine the model fit of the results, but the data fit can be computed by forward modelling. This procedure shows that the travel time and phase delay data are explained quite well by both methods.				
14. SUBJECT TERMS Seismic diffraction tomography Seismic source discrimination Azimuth anomalies			15. NUMBER OF PAGES 72 16. PRICE CODE	
17. SECURITY CLASSIFICATION OF REPORT Unclassified	18. SECURITY CLASSIFICATION OF THIS PAGE Unclassified	19. SECURITY CLASSIFICATION OF ABSTRACT Unclassified	20. LIMITATION OF ABSTRACT SAR	

On the other hand, ordinary tomography is not doing well in explaining the amplitudes, whereas diffraction tomography explains about 20% even when amplitude data are not used in the inversion, and about 40% when the inversion does include these data. It is concluded that the modified method of diffraction tomography described in this paragraph promises to become an important tool for determining the structure beneath seismic arrays.

In paragraph 2.2, the problem of discriminating between earthquakes and underground explosions is formulated as an exercise in pattern recognition approach analysis. The analysis has been applied to a learning set of 44 nuclear explosions (8 test sites) and 35 earthquakes in Eurasia recorded at the NORESS array. The signal features considered were the normalized power in 8 spectral bands in the 0.2-5.0 Hz range of the P-wave (6 sec) and the P-coda (30 sec). Physically, it means that we exploit potential differences in the shape of earthquake and explosion spectra, respectively. Other features included are peak P and P-coda amplitude frequencies and relative P/P-coda power. These 19 features were extracted either from conventional array beam traces or the optimum group filtered traces (OGF-removal of coherent low-frequency noise). Using the feature selection algorithm, based on estimates of the expected probability of misclassification (EPMC), only 2 to 4 features were needed for optimum discrimination performance. The dominant features were coda excitation and P- and P-coda power at lower signal frequencies. Furthermore, feature parameters extracted from the OGF traces had a slightly better performance in comparison to those extracted from beam traces. Finally, there were no misclassifications for OGF-derived features when the explosion population was limited to E. Kazakh, while including events from the other test sites lead to a decrease in discrimination power.

We have previously applied the ray tracing technique of Bostock and Kennett (1990) to the characterization of Lg propagation to the NORESS array. In paragraph 2.3, we have considered the application of the same approach of representing the major features of the Lg phase via constructively interfering S waves multiply reflected within the earth's crust to understanding azimuth anomalies observed at the ARCESS array. The motivation for the theoretical modelling has been the rapid changes in both size and sign of ARCESS Lg azimuth anomalies with geographical position, clearly observed in IMS analysis of events to the south and east of Finland (Gulf of Estonia - Leningrad - USSR north of Leningrad). Theoretical azimuth anomalies calculated from this ray tracing scheme, and based on a simplified model of the Moho structure under the Fennoscandian region, are found to be generally consistent with the trends in the observed anomalies at ARCESS. However the

ray picture for Lg is probably more valuable for providing a tool to investigate the sensitivity of guided wave propagation to the relative position of the source and major subsurface features such as the significant Moho topography under Finland.

Paragraph 2.4 is a contribution on the use of Lg as a yield estimation tool. In recent years, the Lg phase has emerged as maybe the most promising tool to obtain precise yield estimates by seismic means. The pioneering work by Otto Nuttli of Saint Louis University in the early 1970s using readings exclusively from analog seismograms first focused attention on using the Lg phase for seismic source size estimation. With the emergency of widespread digital recordings in the 1980s, the focus shifted to automatic digital processing, using in particular RMS measurements of digitally filtered traces (typically 0.6-3.0 Hz) in a fixed time window (typically 2 minutes). This method allowed reliable estimates to be made even at very low SNR, by using a noise compensation procedure. Thus, NOR-SAR and Grafenberg array measurements of Lg waves from the Shagan River area were sufficiently precise to allow a systematic P-Lg magnitude bias to be identified between the NE and SW parts of that site. Available yield data from Soviet sources indicate that Lg magnitudes show the best consistency with yield for explosions from this area. Most of the evidence for the "stability" of Lg magnitudes is indirect. By pairwise comparison of RMS Lg for a number of different source-receiver paths, it has been demonstrated that single-station RMS Lg can be used to estimate relative magnitude with a remarkably small scatter (0.02-0.03 in  $m_b$  units orthogonally). This was first shown for Semipalatinsk explosions, but has recently been confirmed also for explosions at Novaya Zemlya. The latter observation is particularly interesting, since many of the paths exhibited significant "Lg blockage" effects. Lg waveforms cannot at present be modelled with the same quality of fit between synthetics and data that has been attained with other phases, and many aspects of Lg generation and propagation characteristics are still not well understood. Among topics that need further study are Lg blockage and scattering effects caused by tectonic heterogeneities and the effects of topography, near source geology and depth of burial on Lg excitation. Much challenging work therefore remains to be done in this field.

## Preface

Under contract No. F49620-C-89-0038, NTNF/NORSAR is conducting research within a wide range of subjects relevant to seismic monitoring. The emphasis of the research program is on developing and assessing methods for processing of data recorded by networks of small-aperture arrays and 3-component stations, for events both at regional and teleseismic distances. In addition, more general seismological research topics are addressed.

Each quarterly technical report under this contract presents one or several separate investigations addressing specific problems within the scope of the statement of work. Summaries of the research efforts within the program as a whole are given in annual technical reports.

This Scientific Report No. 11 is the annual technical report for the period 1 October 1990 - 30 September 1991. It contains four separate contributions, and also abstracts for the investigations submitted as quarterly technical reports during FY91.

NORSAR Contribution No. 453

<b>Accession For</b>	
NTIS GRA&I	<input checked="checked" type="checkbox"/>
DTIC TAB	<input type="checkbox"/>
Unannounced	<input type="checkbox"/>
Justification	
By	
Distribution/	
Availability Codes	
Dist	Avail and/or Special
A-1	

---

Table of Contents

1.	Summary	1
2.	Summary of Technical Findings and Accomplishments	3
2.1	Seismic diffraction tomography of array data	3
2.2	Enhanced seismic source discrimination using NORESS recordings from Eurasian events	15
2.3	Ray-based investigation of LG azimuth anomalies at ARCESS'	36
2.4	Lg as a yield estimation tool	46
2.5	Summaries of Quarterly Technical Reports submitted	57



# 1 Summary

This Annual Technical Report describes the work accomplished under Contract No. F49620-C-89-0038 during the period 1 October 1990 - 30 September 1991. The report contains four separate contributions (paragraphs 2.1 through 2.4), and in addition abstracts of the investigations submitted as quarterly technical reports during FY91 (paragraph 2.5).

The inversion of NORSAR travel time data constituted one of the first examples of seismic tomography. It is now becoming apparent that these data are influenced by wave diffraction effects, and hence that ordinary (ray based) tomography may be inadequate. In paragraph 2.1 we apply a newly developed tomographic method that takes diffraction effects into account. Data from the NORSAR array in its original form (22 subarrays; aperture 100 km) have been used and results are compared with those of the ray-based inversion experiments undertaken around 15 years ago. To facilitate comparison with earlier results, we inverted for velocity structure in the same box-like structure as was used in the previous investigations. As we do not know the true structure beneath NORSAR, we cannot determine the model fit of the results, but the data fit can be computed by forward modelling. This procedure shows that the travel time and phase delay data are explained quite well by both methods. On the other hand, ordinary tomography is not doing well in explaining the amplitudes, whereas diffraction tomography explains about 20% even when amplitude data are not used in the inversion, and about 40% when the inversion does include these data. It is concluded that the modified method of diffraction tomography described in this paragraph promises to become an important tool for determining the structure beneath seismic arrays.

In paragraph 2.2, the problem of discriminating between earthquakes and underground explosions is formulated as an exercise in pattern recognition approach analysis. The analysis has been applied to a learning set of 44 nuclear explosions (8 test sites) and 35 earthquakes in Eurasia recorded at the NORESS array. The signal features considered were the normalized power in 8 spectral bands in the 0.2-5.0 Hz range of the P-wave (6 sec) and the P-coda (30 sec). Physically, it means that we exploit potential differences in the shape of earthquake and explosion spectra, respectively. Other features included are peak P and P-coda amplitude frequencies and relative P/P-coda power. These 19 features were extracted either from conventional array beam traces or the optimum group filtered traces (OGF-removal of coherent low-frequency noise). Using the feature selection algorithm, based on estimates of the expected probability of misclassification (EPMC), only 2 to 4 features were needed for optimum discrimination performance. The dominant features were coda excitation and P- and P-coda power at lower signal frequencies. Furthermore, feature parameters extracted from the OGF traces had a slightly better performance in comparison to those extracted from beam traces. Finally, there were no misclassifications for OGF-derived features when the explosion population was limited to E. Kazakh, while including events from the other test sites lead to a decrease in discrimination power.

We have previously applied the ray tracing technique of Bostock and Kennett (1990) to the characterization of Lg propagation to the NORESS array. In paragraph 2.3, we have considered the application of the same approach of representing the major features of the Lg phase via constructively interfering S waves multiply reflected within the earth's crust

to understanding azimuth anomalies observed at the ARCESS array. The motivation for the theoretical modelling has been the rapid changes in both size and sign of ARCESS Lg azimuth anomalies with geographical position, clearly observed in IMS analysis of events to the south and east of Finland (Gulf of Estonia - Leningrad - USSR north of Leningrad). Theoretical azimuth anomalies calculated from this ray tracing scheme, and based on a simplified model of the Moho structure under the Fennoscandian region, are found to be generally consistent with the trends in the observed anomalies at ARCESS. However, the ray picture for Lg is probably more valuable for providing a tool to investigate the sensitivity of guided wave propagation to the relative position of the source and major subsurface features such as the significant Moho topography under Finland.

Paragraph 2.4 is a contribution on the use of Lg as a yield estimation tool. In recent years, the Lg phase has emerged as maybe the most promising tool to obtain precise yield estimates by seismic means. The pioneering work by Otto Nuttli of Saint Louis University in the early 1970s using readings exclusively from analog seismograms first focused attention on using the Lg phase for seismic source size estimation. With the emergency of widespread digital recordings in the 1980s, the focus shifted to automatic digital processing, using in particular RMS measurements of digitally filtered traces (typically 0.6-3.0 Hz) in a fixed time window (typically 2 minutes). This method allowed reliable estimates to be made even at very low SNR, by using a noise compensation procedure. Thus, NOR-SAR and Grafenberg array measurements of Lg waves from the Shagan River area were sufficiently precise to allow a systematic P-Lg magnitude bias to be identified between the NE and SW parts of that site. Available yield data from Soviet sources indicate that Lg magnitudes show the best consistency with yield for explosions from this area. Most of the evidence for the "stability" of Lg magnitudes is indirect. By pairwise comparison of RMS Lg for a number of different source-receiver paths, it has been demonstrated that single-station RMS Lg can be used to estimate relative magnitude with a remarkably small scatter (0.02-0.03 in  $m_b$  units orthogonally). This was first shown for Semipalatinsk explosions, but has recently been confirmed also for explosions at Novaya Zemlya. The latter observation is particularly interesting, since many of the paths exhibited significant "Lg blockage" effects. Lg waveforms cannot at present be modelled with the same quality of fit between synthetics and data that has been attained with other phases, and many aspects of Lg generation and propagation characteristics are still not well understood. Among topics that need further study are Lg blockage and scattering effects caused by tectonic heterogeneities and the effects of topography, near source geology and depth of burial on Lg excitation. Much challenging work therefore remains to be done in this field.

## 2 Summary of Technical Findings and Accomplishments

### 2.1 Seismic diffraction tomography of array data

#### *Introduction*

Seismic tomography has become a widely applied method to determine the crustal and lithospheric velocity structure beneath an array. Actually, different inversion algorithms are being applied, but they all invert travel time data by linearizing the problem, appealing to Fermat's principle. Apart from its inherent scientific interest, the result can be used to interpolate travel time residuals; as such, tomographic results are also of operational interest.

Despite the widespread application of the method, a number of limitations were recognized at an early stage. A fundamental limitation is due to the neglect of wave diffraction off the geometrical ray path. This neglect limits the resolution of tomographic results in general. The limitation is especially serious in circumstances where diffraction effects dominate the observations, as may be expected in the presence of low velocity regions among others. Another practical problem is that seismic tomography operates under the assumption of travel time data representing first arrivals, but these are usually not observable. Instead one measures detection times, or alternatively at an array, one may identify relative time delays with the waveform correlation lags between sensors. In either case, diffraction may significantly affect the data. Diffraction effects have been taken into account, in a first-order approximation, in methods called diffraction tomography (e.g., Devaney, 1984). Unfortunately, the first-order approximation does not adequately recover the phase and hence the travel time residual (although the so-called Rytov approximation has been designed to improve this). Another general problem is that non-physical diffraction from the boundary of the region under study may interfere with the solution (unless the velocity perturbation is zero outside this region). Finally, current methods of diffraction tomography assume a homogeneous background medium and regular sampling of the wave field, such that Fourier transform methods can be used for the solution of the scattering problem at hand. In its present form these methods are of limited use, at least in earthquake seismology.

We have experimented with a new formulation that combines diffraction with ordinary seismic tomography (Doornbos, 1991), overcoming the problems mentioned above. We anticipate that the method can be applied to a range of problems, including for example cross-well tomography. However, the experiment we describe here involves data from the NORSAR array in its original (large aperture) configuration. It is of interest to note that the travel time data from this array have been used in one of the first applications of seismic tomography (Aki et al, 1977), although at the time the inverse method was not called tomography. Thus our experiment naturally leads to a comparative study of diffraction and ordinary tomography applied to teleseismic array data.

### *Outline of theoretical background*

The basis of ordinary seismic tomography is the simple relation, in the ray approximation:

$$\delta\tau \equiv \int_{\text{ray}} \delta s \, d\sigma \quad (1)$$

Here  $\delta\tau$  is the change of travel time  $t$  due to a slowness perturbation  $\delta s$  along the ray, and using Fermat's principle, the integration is along the ray path in the unperturbed reference structure. The ray approximation thus predicts a time shift of the reference pulse:

$$u(t) \equiv u_o(t - \delta\tau) \quad (2)$$

Diffraction theory, on the other hand, predicts

$$u(t) \equiv u_o(t) + \delta u(t) \quad (3)$$

and the linear (Born) approximation for  $\delta u$  is of the form

$$\delta u(t) \equiv \int_V \dot{F}(c, \rho, G, u_o) \delta s \, dV \quad (4)$$

For example, for an acoustic medium with velocity  $c$ , density  $\rho$  and Green's tensor  $G$ :

$$F = -2\rho c G^* \dot{u}_o \quad (5)$$

Upon inspecting equations (2), (3) and (4), one may anticipate the following problems:

(1) If the perturbed structure is relatively smooth, permitting the ray approximation (2), then from (3):

$$\delta u(t) \equiv -\dot{u}_o(t) \delta\tau$$

and this is obviously a poor approximation if  $\delta\tau$  is no longer small.

(2) Inverting equation (4) implies the assumption  $\delta s = 0$  outside  $V$ , causing numerical diffraction if in fact  $\delta s \neq 0$  outside  $V$ .

In view of the above it certainly would be an advantage to relate the perturbation term to the time-shifted pulse:

$$u(t) = u_o(t - \delta\tau) + \delta u_d(t - \delta\tau) \quad (6)$$

provided there exists a sufficiently simple relation between  $\delta u_d$  and  $\delta s$ . Such a relation was derived by Doornbos (1991):

$$\delta u_d \equiv \int_V F \left( \frac{p^o - p^1}{|p^o - p^1|^2} \cdot \nabla \delta s \right) dV \quad (7)$$

where  $p^0, p^1$  are the slowness vectors of the incident and scattered wave, respectively. Equation (7) is linear in the slowness gradient, and any of the velocity or slowness parameterization schemes in common use will convert it to a form that is linear in the slowness itself, so that standard inverse methods can be applied. The common case of a block parameterization is special in the sense that the diffraction term contributes only diffractions from the block boundaries:

$$\delta U_d \equiv \sum_j \sum_{k > j} [\delta s]_k^j \int_{S_{jk}} F \left( \frac{p^0 - p^1}{|p^0 - p^1|^2} \cdot n_{jk} \right) dS \quad (8)$$

where  $S_{jk}$  is the boundary between block  $j$  and  $k$  with normal  $n_{jk}$ , the sum over  $k$  is restricted to blocks adjacent to  $j$ , and the additional restriction  $k > j$  is used to avoid duplicating interfaces.

Writing the perturbation in the form (6) is consistent with the Rytov approximation. The approximation was derived in the frequency domain:

$$\ln \frac{U(\omega)}{U_o(\omega)} \equiv i\omega\delta\tau + \frac{\delta U_d(\omega)}{U_o(\omega)} \quad (9)$$

where  $\delta\tau$  is given by equation (1), and  $\delta U_d$  by the Fourier transform of equation (7) or (8). Equation (9) together with (8) is linear in the slowness perturbation  $\delta s$ ; in practice a solution must be obtained by iteration. Several iteration schemes are possible, but in any case it is important to update the phase delay of the diffracted wavefield in (7). In the present work we use

$$\ln \frac{U(\omega) - U_d(\omega)}{U_o(\omega)} \equiv i\omega\delta\tau + \frac{\delta U_d(\omega)}{U_o(\omega)} \quad (10)$$

where  $U_d(\omega)$  is the diffracted field after the previous iteration, and the phase delay in  $U_d$  and  $\delta U_d$  is updated using the approximation (1).

### *A model experiment*

The model consists of a block-like structure of velocity perturbations. The block size is 20 km, and the velocity varies continuously by  $\pm 3\%$  between blocks, over a gradient zone of about 6 km (Fig. 2.1.1). The size of the whole structure is 200 x 200 km horizontally, and 40 km vertically. The top of the structure is at 80 km depth. An array with the configuration of NORSAR is assumed to record teleseismic P waves coming from different directions, as shown by the slowness diagram of Fig. 2.1.2. The total data set is given by the P waves from 40 events recorded at 22 stations. The incident pulse form is chosen to be similar to a typical teleseismic record. Synthetic waveforms were generated by a combination of 3-D dynamic ray tracing and Kirchhoff-type integration: Rays were traced through the 3-D structure generating the wavefield on an integration surface just above the

top of the structure. The field at the surface was then determined by a Kirchhoff-type of integral over this surface. Relative travel time residuals were determined by correlating the waveforms at the 22 stations with an array beam. These residuals form the data set for ordinary tomography based on equation (1). The waveform spectrum  $U(\omega)$  was also determined for each station, together with the array beam spectrum  $U_o(\omega)$ . The imaginary part of  $\ln(U/U_o)$  in equation (9) gives the phase delay spectrum, which is the counterpart of the travel time residual  $\delta\tau$ . Inversion of the phase delay spectra (that is, operating on the imaginary part of equation (9)) constitutes the central part of diffraction tomography. In this experiment we inverted for 6 frequencies in the band 0.6-2.1 Hz. Simultaneous inversion of the amplitude spectra (the real part of equation (9)) is expected to increase stability of the results.

Obviously, the model considered here is not meant to be a realistic model of Earth structure. Rather it serves as a test to evaluate the inversion algorithm, and it allows a comparison of different tomographic methods under controlled circumstances. The model is special in its regular sequence of low and high velocity regions. Diffraction around the low velocity regions tends to mask the signal from such regions in the travel time data. This process is particularly effective if the size of a region is of the order of a Fresnel zone; the scaling of our experiment was in fact designed to match this condition. Another special feature of our experiment is that in the inversion we choose the block parameterization to match the block size structure of the model. This will minimize the smoothing of tomographic results, but it will also emphasize errors in these results.

Under these special conditions, ordinary tomography does indeed produce relatively large errors. We define a measure of the normalized squared error:

$$\epsilon = \frac{\int_V (\delta c - \hat{\delta c})^2 dV}{\int_V (\delta c)^2 dV} \quad (11)$$

where  $\delta c$  is the model velocity perturbation and  $\hat{\delta c}$  is its estimate. The values for  $\epsilon$  depends on how strongly we damp the solution, but for ordinary tomography we always find  $\epsilon > 100\%$ . For diffraction tomography we get  $\epsilon \approx 35\%$ . The error is largest near the boundary of the model. Deleting from integration (11) the blocks along the boundary reduces  $\epsilon$  to 25%. This represents a significant improvement over ordinary tomography. For other, smoother models, the improvement would of course be less dramatic.

#### *Application to the NORSAR array*

The geometry of the experiment is illustrated in Fig. 2.1.3. To facilitate comparison to earlier results, we invert for velocity structure in the same box-like region as Aki et al (1977) and we use the same block parameterization. However, to more fully include the diffracted field we extended the box size slightly horizontally. The size was 220 x 220 km horizontally and 126 km vertically, layer thicknesses were 17, 19, 30, 30 and 30 km, and the block size within each layer was 20 x 20 km horizontally. We also use the same basic data set, retaining the data from 86 events. The P slowness solutions from these events are shown in Fig. 2.1.4. Clearly, sampling of the structure is very non-uniform; in particular the southern part of the structure is poorly sampled by rays. It is well-known that non-uniform

sampling tends to deteriorate tomographic results, but this problem would be less severe for diffraction tomography due to the additional constraint by the diffraction term (equation 7). An example of the result for one of the layers (the depth range 66-96 km) is shown in Fig. 2.1.5 for ordinary tomography, and in Fig. 2.1.6 for diffraction tomography. Ignoring the prominent features near the boundary of the grid as possibly due to numerical boundary diffraction, the pattern near the center of the grid shows about  $\pm 6\%$  velocity perturbations for both methods. Details of the two results are different however. We do not know the true structure so we cannot determine the model fit of the results, but we can compute the data fit. Synthetic data were constructed after forward modelling the diffracted field using a first-order (Rytov) approximation and adjusting the phase delay. A summary of results is shown in Fig. 2.1.7a for different types of data (travel time residuals, phase delays and amplitudes). Clearly the travel time and phase delay data are explained quite well by both methods. On the other hand, ordinary tomography is not doing well in explaining the amplitudes; diffraction tomography explains about 20% even when amplitude data are not used in the inversion, and about 40% when the inversion does include these data. In a further test we inverted the synthetic data for one of the models (from diffraction tomography: DT, p&a of Fig. 2.1.7a). This produces a measure of model fit in addition to the data fit, for the different methods of tomography. The results are summarized in Fig. 2.1.7b. The general features of the data fit are similar to those for real data. Ordinary tomography produces a very poor fit to the true model, but diffraction tomography reduces the model fit error  $\epsilon$  (equation 11) to about 30%. Of course this may be an overly optimistic result since the forward and inverse method were based on the same approximation, but the results do agree with those of the model experiment described earlier. The modified method of diffraction tomography described here thus promises to become an important tool for determining the structure beneath seismic arrays.

**E. Ødegaard**  
**D.J. Doornbos**

#### *References:*

- Aki, K., A. Christoffersson and E.S. Husebye (1977): Determination of the three-dimensional structure of the lithosphere, *J. Geophys. Res.*, 82, 277-296.
- Devaney, A.J. (1984): Geophysical diffraction tomography, *IEEE Trans. Geosc. Rem. Sens.*, GE22, 3-13.
- Doornbos, D.J. (1991): Diffraction and seismic tomography, *Geophys. J. Int.*, in press.

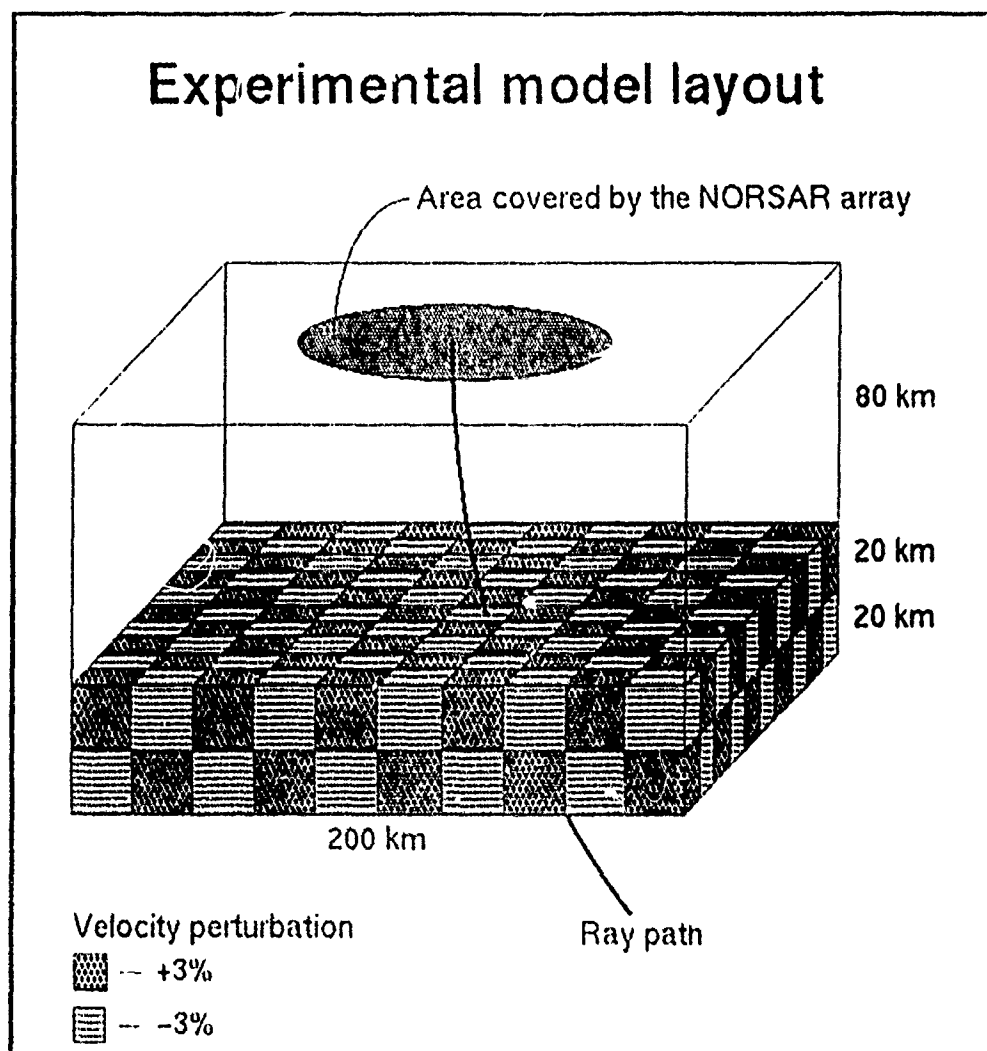


**Fig. 2.1.1.** Model velocity structure, with location of receiver array indicated. The continuous velocity variation between blocks is not shown in this figure.



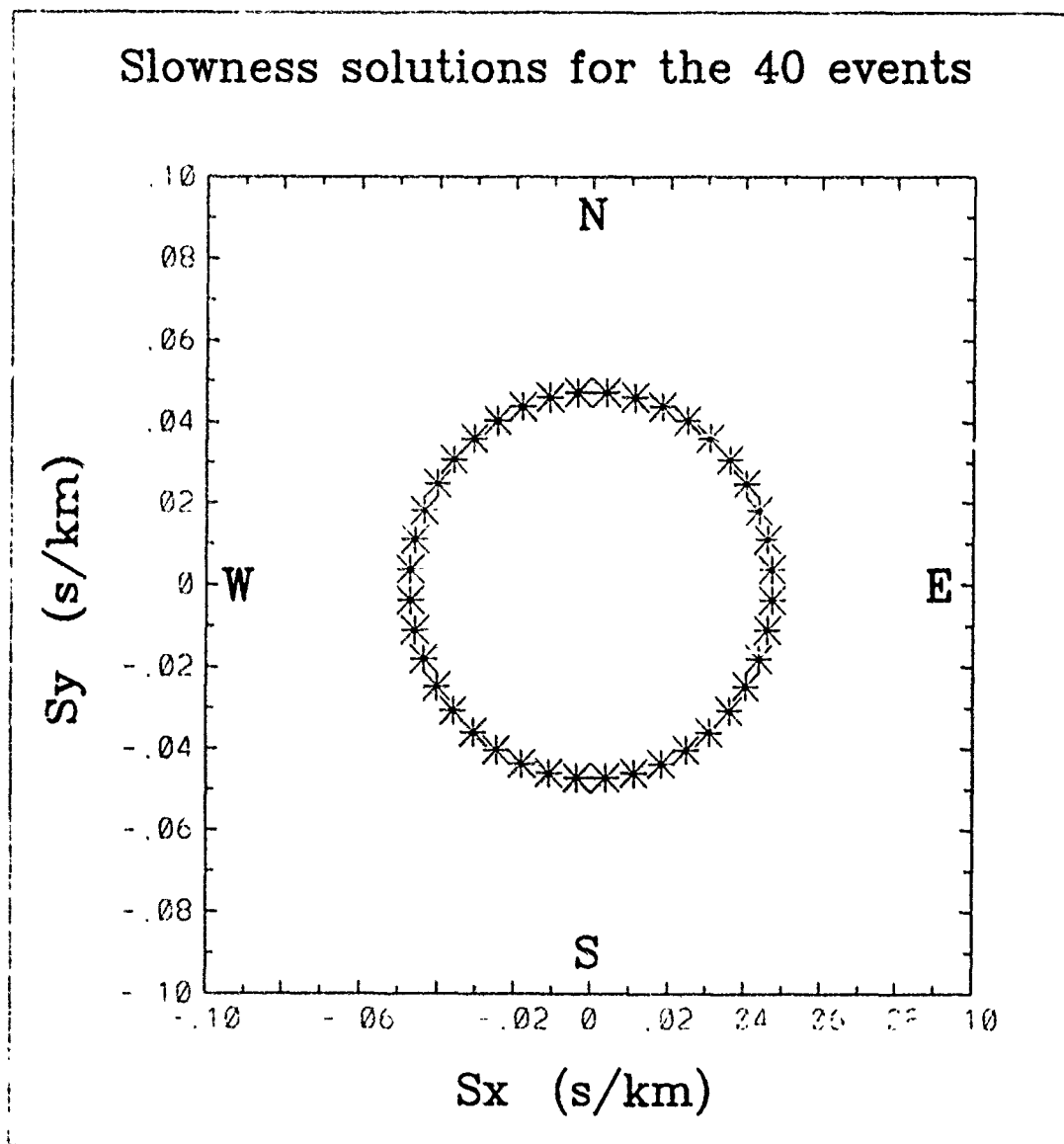
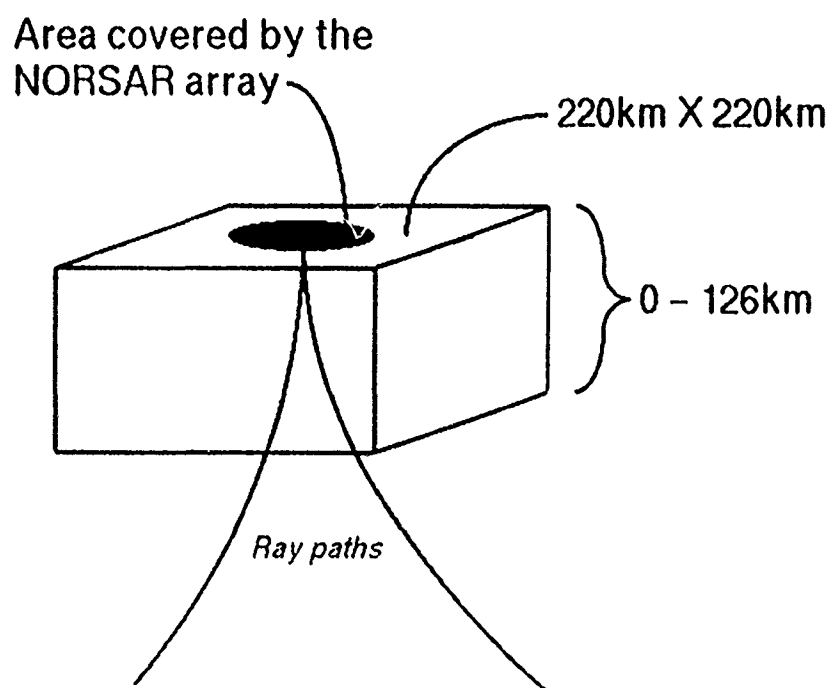
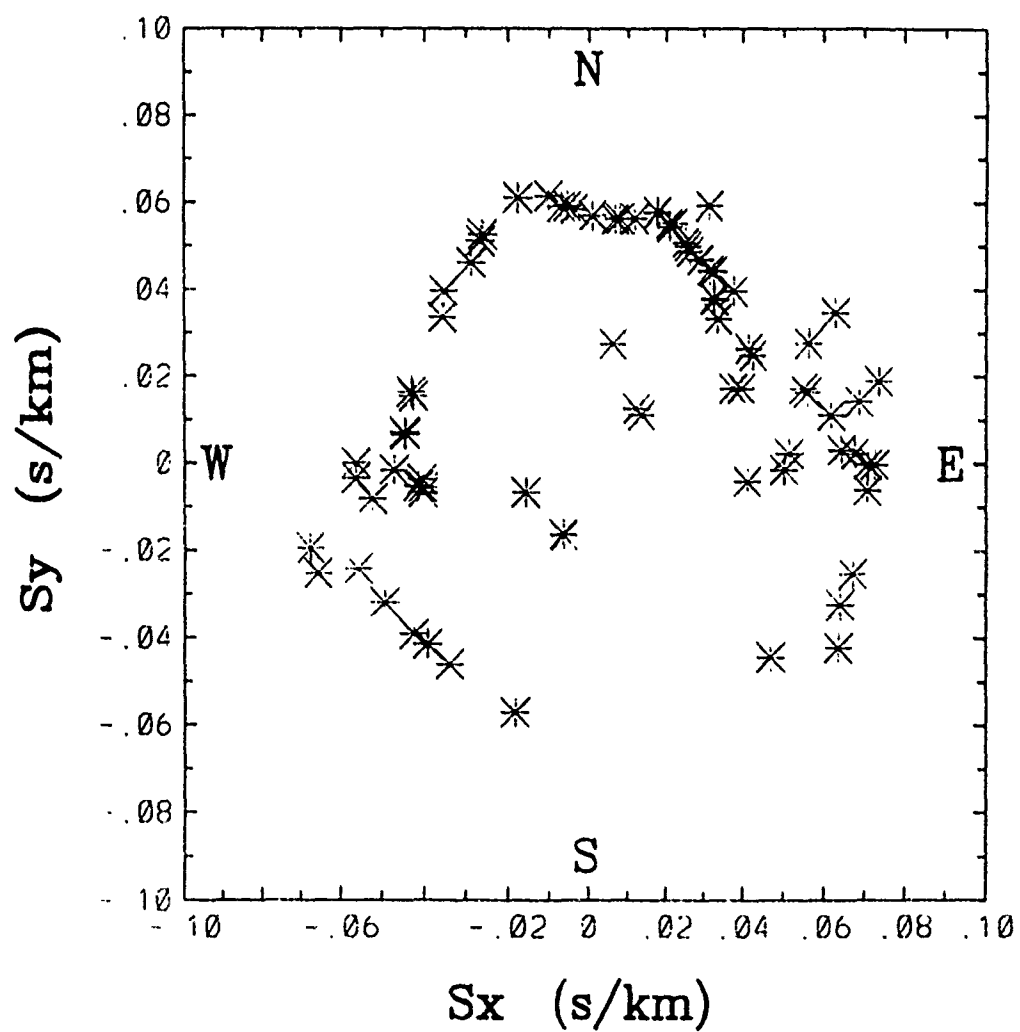


Fig. 2.1.2. Slowness of P phases used for model experiment.



**Fig. 2.1.3.** Sketch of inversion experiment at NORSAR.

## Slowness solutions for the 86 events

**Fig. 2.1.4.** Slowness of P waves used for inversion experiment at NORSAR.

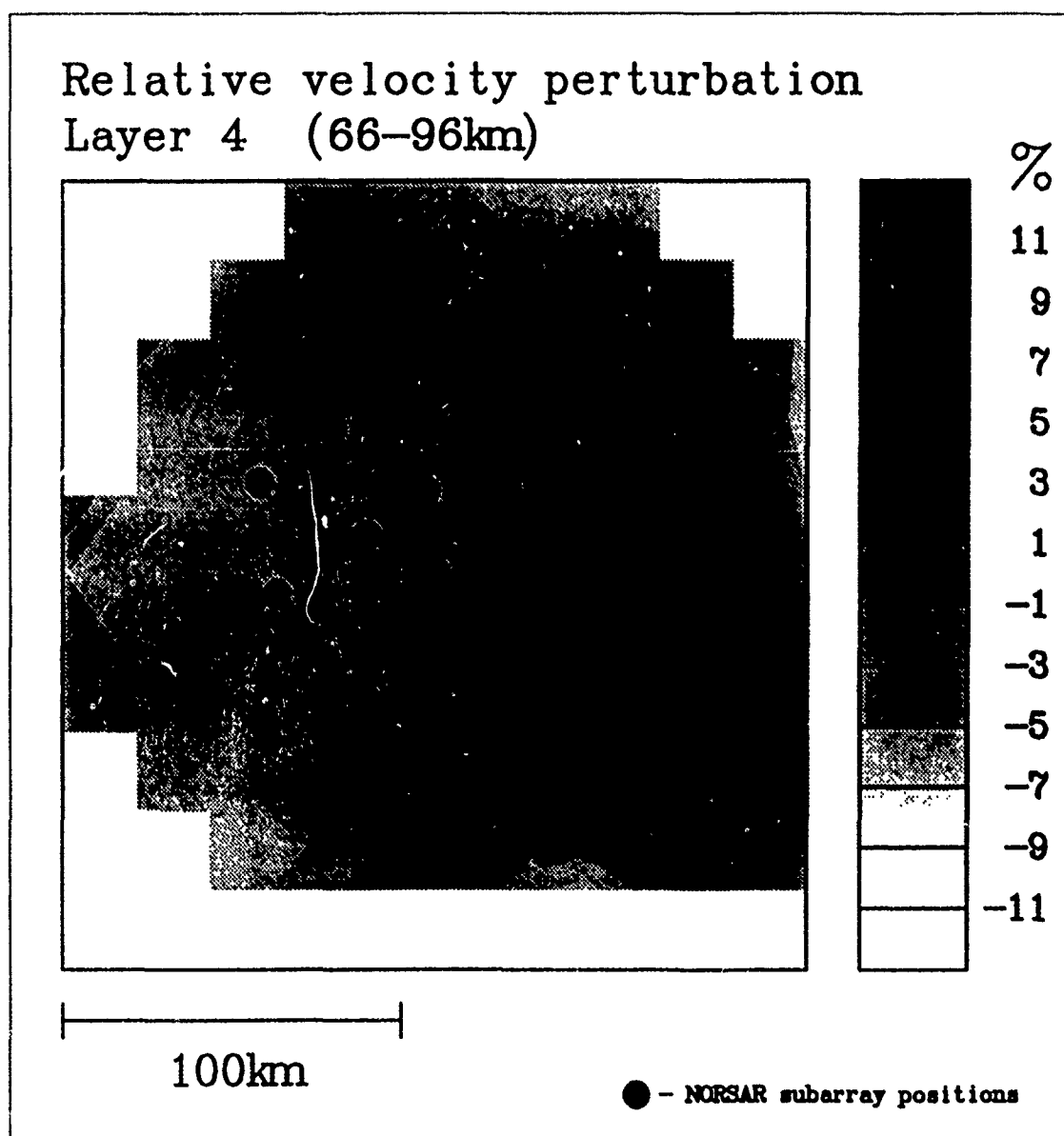


**Fig. 2.1.5.** Velocity perturbations for layer 4 (66–96 km). Results from ordinary tomography. Open fields are not sampled by rays.

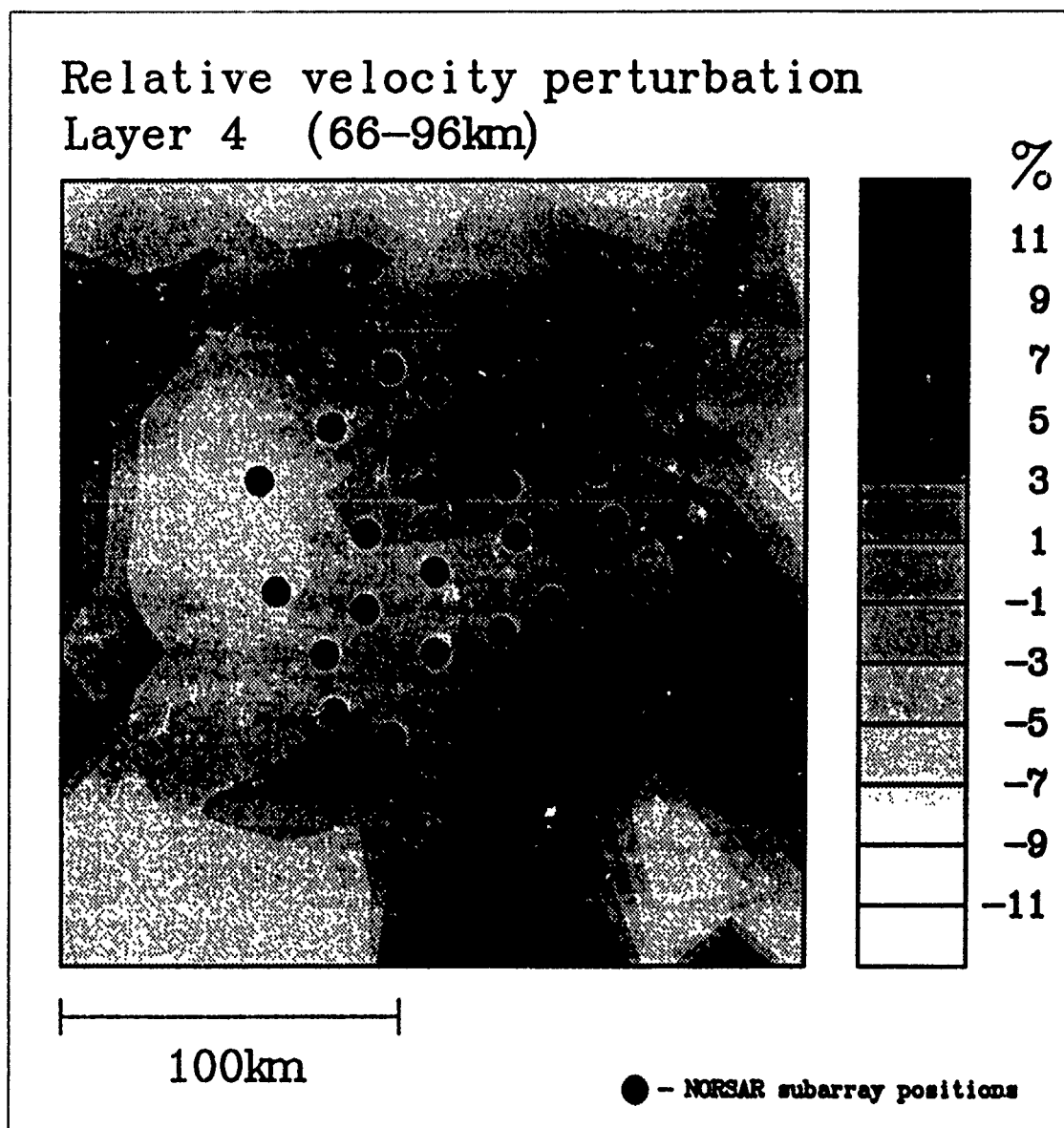
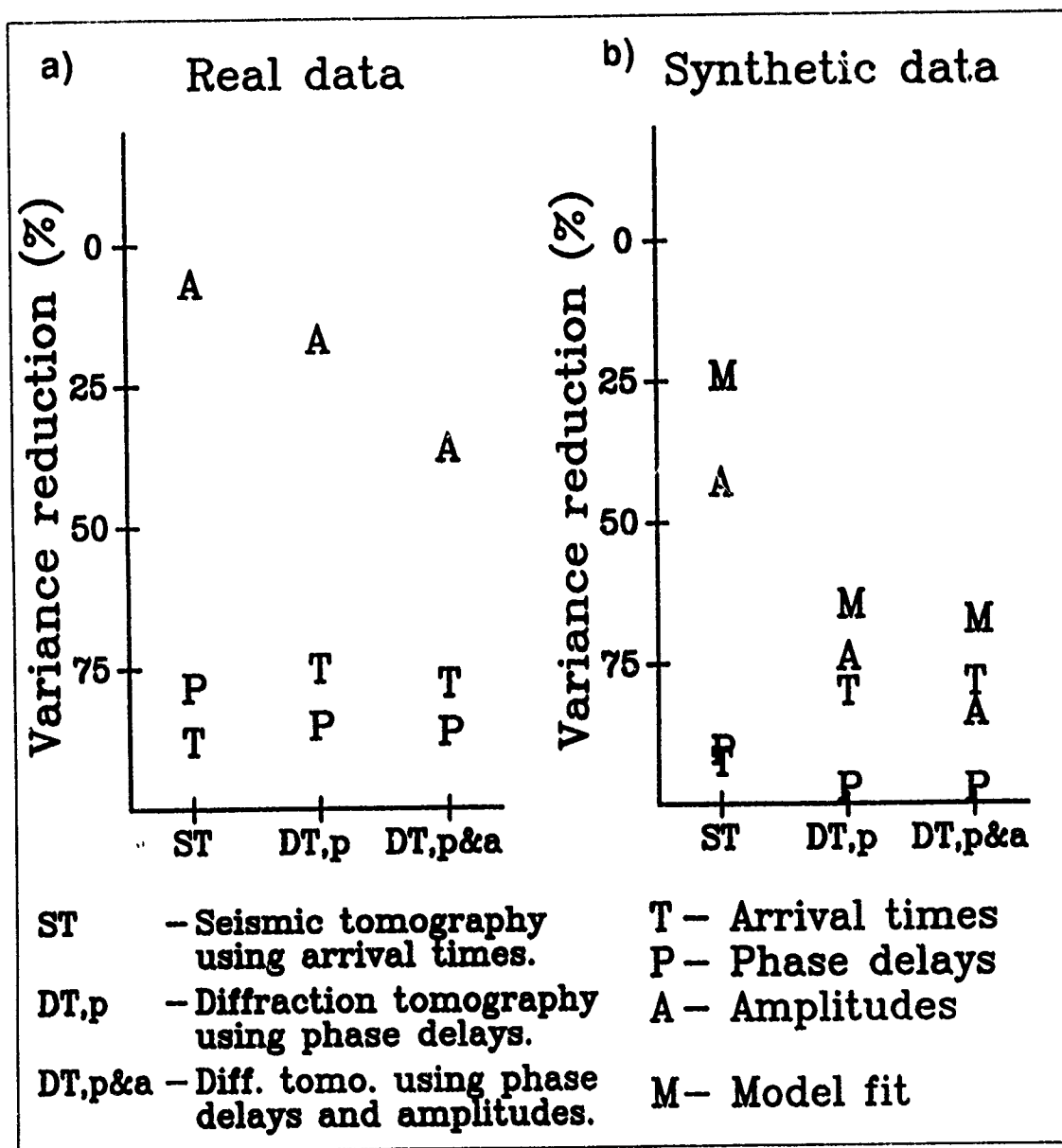


Fig. 2.1.6. Velocity perturbations for layer 4 (66–96 km). Results from diffraction tomography.



**Fig. 2.1.7a** (left): Data fit after tomography at NORSAR. ST: Ordinary tomography. DT, p and DT, p&a: Diffraction tomography without and with amplitude data. **b** (right): Data and model fit after tomography with synthetic data at NORSAR. Synthetics were generated for model DT, p&a.

## 2.2 Enhanced seismic source discrimination using NORESS recordings from Eurasian events

### *Introduction*

The problem of distinguishing underground nuclear explosions from natural earthquakes using seismic data has been studied for a long time. In fact, it dates back to 19 sep 1957 as on that day a nuclear explosion, code-named Rainier, was detonated under the Nevada desert. In order to avoid the once troublesome issue of in-country operation of non-national seismic stations, the source identification research in the 1960 and 1970-ties focused on observations in the teleseismic window. The most successful criteria for seismic source identification were spectral ratio variants, mainly between non-overlapping frequency bands for the P-signal itself, or the relative signal excitation at 1 sec (P-wave) and 20 sec (surface waves). The latter is often denoted the  $m_b:M_s$  (body wave versus surface wave magnitudes) discriminant. Another commonly used discriminant was the so-called complexity tied to the ratio of P coda RMS in two consecutive windows of lengths around 5 sec and 30 sec respectively (Dahlman and Israelson, 1977). A variant of the complexity often denoted the coda discriminant, was introduced by Tjøstheim (1975, 1978) and Sandvin and Tjøstheim (1978) using autoregressive spectral coefficients as signal attributes in combination with more advanced discrimination statistics. Recently, new concepts have been introduced, namely, the so-called artificial or trained neural networks technique (e.g. see Dowla et al, 1990 and Dysart and Pulli, 1990).

In this study we address the problem of teleseismic source discrimination and explore the potential of the spectral ratio and complexity discriminants. We use data from the NORESS array, which has an excellent detectability for events in parts of Eurasia.

### *Event selection and NORESS record preprocessing*

The presumed earthquakes (PDE and ISC listings) and presumed underground nuclear explosions (NORSAR listings) used in this study are listed in Tables 2.2.1 and 2.2.2 and depicted in Fig. 2.2.1 as well. Most of the explosions (32 out of 44) stem from the E. Kazakh (Semipalatinsk) test site and hence the earthquakes in the  $m_b$  range 4.0 to 6.0 were selected from the same general area. The other test sites are in aseismic areas for which sufficient earthquake recordings are not available. However, the outlying explosions were included for a check on discriminant robustness. A simple and efficient scheme for SNR enhancement is delay-and-sum processing or beamforming which is most efficient in the 2-8 Hz band. At lower frequencies (below say 2 Hz) the wavelengths of microseisms are of the same order as the array aperture, and hence strong correlation in the noise across the array is often observed. In such cases Ingate et al (1985) demonstrated the usefulness of maximum likelihood schemes for suppressing correlated noise. Recently, even more advanced methods have been introduced by Kushnir et al (1990), which are extensively used here for suppressing low frequency propagating noise. The efficiency of this scheme, commonly denoted the Optimal Group Filtering (OGF) technique is demonstrated in Fig. 2.2.2. Naturally, removal of low frequency noise is important as both theoretical and observational studies demonstrate that part of the discrimination power is

vested in the low/high frequency bands of the P-signal (Evernden et al, 1986). Evernden (1977) advocates the use of P-signal frequencies up to 9 Hz in teleseismic discrimination studies, while we restricted the analysis to 5 Hz. Our rationale being that there is not much signal energy above 5 Hz and besides cultural sources like local quarry blasting, mining explosions and fast running machinery (saw mills) could easily bias the observational data. In short, our discriminant parameters were extracted both from single P-beam traces and from OGF traces in order to have observations for judging the relative importance of the latter.

#### Signal attributes - class of wavefield parameters for discrimination

As mentioned, the most powerful discrimination parameters are related to differential signal excitation in different frequency bands for earthquakes and explosions respectively. P-wave parameters are an obvious choice here, because this phase is most easily detected. Coda waves are interesting as they not only reflect the source but also the source location within the crust/upper mantle. For example, coda excitation and duration are far less efficient for surface explosions and deep earthquakes relative to shallow and intermediate depth earthquakes (Dainty, 1990). Rayleigh waves are not considered simply because they become embedded in background noise for event  $m_b$  magnitudes at 4.5 - 5.0 or below. The essence of the above discussion is that our class of discrimination parameters is tied to the P-signal and its coda as illustrated in Figs. 2.2.3 and 2.2.4. The choice of window lengths of 6 sec and 30 sec reflects that most of the desirable information from teleseismic, but also regional events are accumulated in the first 3 - 6 sec of the P-wave and then the subsequent 10 - 30 sec coda waves where scattering contributions are still significant.

Processing details were as follows. For each event 5 minutes of recordings for all 25 vertical NORESS sensors were extracted. The first 2 minutes of pure noise were used for estimating OGF-filter coefficients for the slowness and azimuth of the individual events. After the filtering was performed, amplitude spectra (FFT) were calculated for the P-signal (6 sec) and the P coda (30 sec). The power spectrum for the non-overlapping 8 bands specified in Figs. 2.2.3 were obtained by simple averaging of spectral squared amplitudes. Since the events used in analysis have widely different magnitudes, all power spectra were normalized by their maximums. Physically, this means that potential spectral shape differences are exploited for event discrimination purposes. The final feature parameter values were obtained by taking the logarithm of the normalized spectral values. As shown in Fig. 2.2.3 we have 8 feature parameters for both the P signal and the P coda for the same set of frequency bands. Additional parameters introduced (nos. 17 and 18) are peak spectral frequencies and finally the 19th parameter being the ratio of P/P coda spectral maxima. Note that the last parameter is close to the classical complexity definition.

#### Discrimination approach

The seismic discrimination undertaking is a two-stage process: firstly, relevant discrimination parameters must be defined and extracted from the records, and secondly, decision rules (discriminators) must be introduced to ensure proper event classification. At the outset of this study, we discussed rather extensively among ourselves which discrimination approach would be best for classification of Eurasian events as recorded by NORESS. The



importance of the physical aspect of the problem at hand was duly recognized, that is, the extracted discrimination parameters must be seismologically relevant. Furthermore, the persistence of the seismic source identification problem is that a unique set of discriminants for weak events apparently does not exist, so we wanted to have the ability to decide statistically which ones of such parameters would be most informative for a given area or region.

The recognition problem in our case may be formulated as follows. The data set consists of three sets. The first two are the sets  $R_1$  of explosions (NE) spectral parameters vectors  $r_i^{(1)}$ , and  $R_2$  earthquake (EQ) spectral parameters vectors  $r_i^{(2)}$ :

$$R_j = \{r_1^{(j)}, \dots, r_{N_j}^{(j)}\}; \quad r_1^{(j)} = (p_1, \dots, p_n); \quad i = 1, 2 \quad (1)$$

$N_j$  - number of observations in the  $j$ -th learning set (earthquakes or explosions),  $j=1,2$

$p_k$  - values of classification features (spectral parameters  $P$  and  $P$ -coda),  $k=1,n$

$n$  - number of classification features.

$R_1$  and  $R_2$  form the learning material for the NE and EQ classification features. The third set is the vector  $X$  containing discrimination parameters for an "unknown" event, i.e., the vector being classified with no prior knowledge as to its source identification. On the basis of the learning samples  $R_1$  and  $R_2$ , we must make a decision on whether  $X$  belongs to the first or the second class. This is done by using a decision (discriminator) function  $g(X, R_1, R_2)$ . The equivalent Bayesian rules are: If  $g(X, R_1, R_2) < C$ , the hypothesis  $H_1$  is correct and  $X$  belongs to the first class; if  $g(X, R_1, R_2) > C$ , the hypothesis  $H_2$  is correct and  $X$  belongs to the second class. Here  $C$  is a constant, that is, a threshold value. Using this decision rule, there are errors of two kinds: the vector  $X$  belongs to the second class (the hypothesis  $H_2$  is correct), while it is assigned to the first class. Errors of the second kind represent the reverse situation. Errors occur because the observations  $R_1, R_2$  and  $X$  are random, measurement errors and the random nature of the discrimination features themselves. The classification errors of the first and second kind are described by the probabilities  $P_1$  and  $P_2$ . It is also assumed that a priori probabilities  $q_j$ ;  $j=1,2$  of the vector  $X$  belonging to the  $j$ -th class are known, and the total error probability  $P_{err} = q_1 P_1 + q_2 P_2$  can then be evaluated. In our case the sizes of the learning samples (35 EQ and 44 NE) are comparable to the dimension  $n$  of the features space (19 spectral parameters). In such cases, it is difficult to resolve the basic classification problem -- to select the optimum decision rule and evaluate its corresponding error probabilities. Since the distribution patterns corresponding to the first and second class are unknown, it is theoretically impossible to construct a uniformly optimum decision rule, which in all cases will yield the least probability  $P_{err}$  of misclassification (Kushnir et al, 1986). A criterion for choosing a particular rule is the requirement of minimizing the probability of misclassification (PMC).

From this point of view, when the  $R_1$  and  $R_2$  distributions are normal, the linear discriminant function (LDF) is optimal in some statistical sense (Anderson, 1958):

$$L(X, R_1, R_2) = (X - 0.5(r_1 + r_2))^* S^{-1}(r_1 - r_2) < C \quad (2)$$

where

$$r_j = 1/N \sum_{i=1}^{N_j} r_j^{(j)}; \quad j = 1, 2$$

$$S = [1/(N_1 + N_2 - 1)] (A_1 + A_2)$$

$$A_j = 1/(N_j - 1) \sum_{i=1}^{N_j} (r_i^{(j)} - r_j) (r_i^{(j)} - r_j)^*$$

$X$  - vector being classified,

$S$  - covariance matrix of learning sets,

$r_j$  - average vector of  $j$ -th learning set,

$C$  - threshold; above is EQ, below is NE

$N_j$  - number of observations in the  $j$ -th learning set

$*$  - matrix transpose.

Note, the LDF expression in eq. (2) is often denoted the Fischer discriminant (Anderson, 1958).

#### Error probability estimation

The principal method of deriving approximate expressions for error probabilities is that of asymptotic representations of the distributions of discriminator statistics. Of major interest in seismic discrimination analysis is the case when  $N$  (number of events in learning sets) and  $n$  (number of features) are of the same order and have double digit values. For LDF the asymptotic equation suggested by Kolmogorov, where the error probabilities are investigated when both  $n$  and  $N$  approach infinity and  $n/N$  is constant, remains approximately valid. Deev (1970) has shown that in Kolmogorov's asymptotic, the distribution of the LDF linear discriminator ( $L$  in eq. (2)) is asymptotically normal with mean  $M$  and variance  $V$ :

$$M_j = [2(N-2)/(2N-1-n)] [(-1)^j V^2/2] \quad j = 1, 2$$

$$V = [(N-1)(2N-1)(2N+1)/(2N-n-1)(2n-n)n] [D^2 + 2n/N] \quad (3)$$

with  $N = N_1 = N_2$ , and  $D^2 = (r_1 - r_2)^* S^{-1} (r_1 - r_2)$ .

From (3), the following approximate expression for the EPMC of the LDF (Linear Discriminant

Function) can be written:

$$\begin{aligned} P1 &= P \{g \leq C | H2\} = G((C - M_1)/V) \\ P2 &= P \{g \geq C | H1\} = G((M_2 - C)/V) \end{aligned} \quad (4)$$

where

$$G(y) = 1/\sqrt{2\pi} \int_{-\infty}^y e^{-x^2/2} dx$$

Raudis and Pikiyalis (1975) have shown that the relative error in evaluating the probability of misclassification yielded by asymptotic expression (4), as compared with the error computed from an exact expression, is not greater than few per cent in the common observation ranges of  $N$  and  $n$ . The event classification strategy as adopted in this study is visualized in Fig. 2.2.5.

Broad practical applications of LDF in various classification problems have confirmed its efficiency for small sizes  $N1$  and  $N2$  of learning samples and for distributions that differ from normal (Azen et al, 1975; Weber et al, 1986; Tsvang et al, 1986). In essence, the advantage of LDF is its simplicity, and the existence of a method for calculating EPMC.

#### Selection of most informative features

As mentioned above, the linear discriminant function has a good performance when the sizes of learning sets are small. LDF can be applied not only to the total number of discriminant features ( $r_1^{(j)}$  in eq. (1)), but also to vectors made up of a subset of the discriminants. Various values of the expected probability of misclassification (eq. (4)).

The natural strategy would be to take only the set of features which represents the minimum of the EPMC. In order to make use of this idea, one must be able to arrange the available features in a sequence such that increasing the set of features by one feature at a time would produce the maximum rate of growth of the function  $D^2(n)$ . One possible way of ranking the features is the following: at each iteration step  $K$  the optimum subset of  $K-1$  features previously selected is increased by adding the one feature from among the remaining set, which yields the largest difference  $D^2(K) - D^2(K-1)$ . The features are thus ranked in significance and in relation to the Mahalanobis distance  $D$  as a function of features  $n$ . Then the EPMC are computed and plotted versus ranked features. The optimal subset of features corresponds to the minimum of EPMC, as illustrated in Fig. 2.2.6.

To provide more confident decision we used also the so-called Jack-knife method, which allows the creation of an independent data set for testing the discriminator without decreasing the learning data set. Here learning and testing are carried out repeatedly: during each learning sequence one element is omitted from the entire sample and in turn used

for testing. The total number of errors is then summarized. In essence, all elements of the sample are used both for learning and testing, but the element being used for recognition are statistically independent of the learning set. Finally, it should be noted that the Jack-Knife method may also be used for estimating the conditional probability of misclassification not the EPMC.

### *Results*

Perhaps the most important aspect of the seismic source identification problem is that of finding proper discriminant parameters. In our case we selected 19 discriminant candidates (Fig. 2.2.3) and have used the Expected Probability of Misclassification Probability (EPMC) measure for ranking the relative importance of these parameters as illustrated in Figs. 2.2.7a and 2.2.7b. In these figures we differentiate between two populations, namely, all events (44 NE and 35 EQ) and only Semipalatinsk explosions and all earthquakes (32 NE + 35 EQ) for OGF (Optimum Group Filtering) and BEAM traces, respectively. Parameter no. 19 (Fig. 2.2.3) are clearly the most dominant for all cases, and thus demonstrate the relevance of the classical complexity discriminant. There appear to be some differences between the OGF and BEAM trace derived parameters, as in the former case the optimum performance (EPMC minimum) is tied exclusively to the coda parameters. For BEAM traces, the classical spectral parameters are of some importance as weight is given to relative signal power in the low frequency bands (parameters 1 and 3 in Fig. 2.2.7a).

The parameters no 10 and 19 derived from OGF traces have clearly the best performance without any misclassification when the NE populations are limited to the E. Kazakh test site (Case 6: Table 2.2.3). The BEAM parameters produce relatively many misclassified explosions, with one exception they stem from the E. Kazakh test site.

Among the earthquakes, no. 26 in Table 2.2.2 appears to be the most problematic, since it is consistently misclassified both by BEAM and OGF parameters, except for one marginal rating in the latter case (Case 6: Table 2.2.3). For other earthquakes being misclassified or given a marginal rating, there is little overlap between the respective OGF and BEAM discriminators. In Fig. 2.2.8 number of events are displayed for which the discriminators were less effective or failed. We would specifically comment on these events in the next section.

### *Discussion*

From Table 2.2.3 we have that the poorest performance takes place for the combination of all events and all discrimination parameters either derived from OGF or BEAM traces. Rather surprisingly, the number of marginal events seemingly is independent of event population and discrimination parameters used. Regarding the misclassified NE populations, most of the events here are non-Semipalatinsk (E. Kazakh), the exception being event 22 (BEAM) and events 18 and 42 (OGF - Case 4: Table 2.2.3). Under optimum conditions (Case 6: Table 2.2.3), event 42 is labelled marginal. From the visual inspections of traces (Fig. 9), some of the failures are rather obvious, but this is not the case for NE 22 (BEAM - Cases 1-3: Table 2.2.3). We note that the two problematic E. Kazakh events, no 22 and 42, are assigned the smallest mb values (Table 2.2.1).

Also some of the presumed earthquakes are problematic, in particular EQ 11, 16 and 26 (Cases 3 and 5; Table 2.2.3). The BEAM and OGF displays in Fig. 2.2.8 give the visual impressions that EQ 11 and 26 exhibit P waves rather typical for explosions. A common feature of the 3 events is their northernmost latitude of  $47^{\circ}$  N, while corresponding longitudes are around  $83.3^{\circ}$ ,  $89.7^{\circ}$  and  $73.6^{\circ}$  E (Table 2.2.2). Also, EQ 26 is weak ( $m_b$  4.3) and besides took place in an area with no previous seismic activity. The ISC bulletins give a normal focal depth of 33 km, and that Garm is the only USSR reporting station.

Note, most discrimination procedures tend to favor a relatively better classification performance for earthquakes as also seen in Table 2.2.3. The reason is that explosion discriminants are tied to relatively weak coda excitation and/or P-signal power deficiency in low frequency bands. For decreasing SNR the noise contribution would be more relatively important for explosions and the net effect is that all weak events would "look" like earthquakes. In the latter case it seems reasonable to select for learning sets weak events only and then take advantage of the OGF-technique for noise suppression.

From the above we have that the performance is best when the two learning populations are drawn from roughly the same area. It is also clear that the discriminators derived from the OGF- traces not surprisingly outperform the corresponding BEAM parameters. This is not surprising for the simple reason that the signal-to-noise ratio is significantly better on the OGF traces (e.g., see EQ 26 in Fig. 2.2.8). Not easily explainable is the fact that the BEAM parameters are weighted in favor of the low frequency part of the P signal, slightly in contrast to that for the OGF parameters.

At the outset of this study the "neural network" approach was not contemplated, and besides Dysart and Pulli (1990) and Dowla et al (1990) reported that the Fisher discriminant had equivalent performances. The reason for this is that the EQ and NE populations are essentially linearly separated. It is here meant that the feature parameters derived from the respective event populations are separated by a straight line in a two parameter case. We would here add that our approach is relatively robust for small-sized event populations and furthermore that the probability of misclassification introduced here is helpful in judging discrimination performances. Further details are given in Tsvang et al (1992).

### *Conclusion*

In this study we have presented a comprehensive seismic source discrimination scheme for NORESS-recorded teleseismic events, comprising 44 nuclear explosions (NE) and 35 earthquakes (EQ) from the general E. Kazakh area. Major results were as follows:

- A total of 19 potential discrimination features were considered. These were mainly tied to normalized spectral power in 8 frequency bands for both P- and P-coda waves of durations 6 sec and 30 sec, respectively. Also, the classical P-complexity discriminant was incorporated.
- The most effective discrimination features were the complexity one, and relatively low P- signal frequencies. The best classification performance was obtained by using 2 to 4 features which in turn were selected on the basis of the extracted measure of maximum misclassification probability.

- The features extracted from the OGF event traces had a slightly better performance than those derived from the conventional event beam traces. The corresponding optimum feature subsets were somewhat different.
- When the explosion population was restricted to the Semipalatinsk area, a complete event classification was obtained using OGF-derived features. However, 3 events here were rated of marginal significance.
- When the explosion population comprised events from an additional 7 testing areas, the classification performances decreased. This is attributed to localized site structures and upper mantle propagation effects.
- A remaining problem is that of designing discriminants for areas where available events are essentially limited to either earthquake or explosion populations.

**S.L. Tsvang, V.I. Pinsky, MITPAN Inst., Moscow**  
**E.S. Husebye**

### *References*

- Anderson, T. W. (1958). Introduction to multivariate statistical analysis, Wiley, New York.
- Azen, S. P., L. Breiman and W. S. Meisel (1975). Modern approaches to data analysis. Course Notes. Technology Service Corporation, Santa Monica, CA.
- Dahlman, O. and H. Israelson (1977). Monitoring of Underground Nuclear Explosions. Elsevier, New York, 440 pp.
- Dainty, A. M. (1990). Studies of coda using array and three-component processing, PAGEOPH, 132, 221-244.
- Deev, A. D. (1970). Representation of statistics of discrete analysis and asymptotic expansion for space dimension comparable with sample size, Dokl. Akad. Nauk, v.195, N 4, USSR, 759-762.
- Dowla, F., S. Taylor and R. Anderson (1990). Seismic discrimination with artificial neural networks: preliminary results with regional spectral data, Bull. Seism. Soc. Am. 80, 1346-1373.
- Dysart, P. S. and J. J. Pulli (1990). Regional seismic event classification at the NORESS array: seismological measurements and the use of trained neural networks, Bull. Seism. Soc. Am. 80, 1910-1933.
- Evernden, J. F. (1977). Spectral characteristics of the P codas of Eurasian earthquakes and explosions, Bull. Seism. Soc. Am., 67, 1153-1171.

- Evernden, J. F., C. B. Archambeau and E. Cranswick (1986). An evaluation of seismic decoupling and underground nuclear test monitoring using high-frequency data, *Rev. Geophys.*, 24, 143-215.
- Ingate, S. F., E. S. Husebye and A. Christoffersson (1985). Regional arrays and optimum data processing schemes, *Bull. Seism. Soc. Am.*, 75, 1155-1177.
- Kushnir, A. F., E. V. Troitskiy and S. L. Tsvang (1986). Dependence of the probability of recognition errors of the size of the sample being classified, *Computational Seismology*, Allerton Press, Inc., 19, 77-82.
- Kushnir, A. F., V. M. Lapshin, V. I. Pinsky, and J. Fyen (1990). Statistically optimal event detection using small array data, *Bull. Seism. Soc. Am.* 80, 1934-1950.
- Raudis, Sh. Yu. and V. S. Pikyalis (1975). Tabulation of the expected classification error of a linear discriminant function as a function of the training sample, In: *Statistical problems of control*, Institute Fiziki i Matematiki AN LitSSR, Vilnius, N 11, 81-120 (in russian).
- Sandvin, O. and D. Tjøstheim (1978). Multivariate autoregressive representation of seismic P-wave signals with application to short-period discrimination, *Bull. Seism. Soc. Am.* 68, N3, 735-756.
- Tjøstheim, D. (1975). Autoregressive representation of seismic P-wave signals with an application to the problem of short-period discriminants, *Geophys. J. R. astr. Soc.* 43, 269-291.
- Tjøstheim, D. (1978). Improved seismic discrimination using pattern recognition, *Phys. Earth Planet. Int.*, 16, 85-108.
- Tsvang, S. L., A. F. Kushnir, S. P. Starodubrovskaya, N. G. Gamburtseva, I. A. Ravich (1986). Statistical Analysis of Wave Tails in Seismic Sounding, *Izvestia, Earth Physics*, 22, 7, 540-552.
- Tsvang, S. L., V. I. Pinsky and E. S. Husebye (1992): Enhanced seismic source discrimination using NORESS recordings from Eurasian events, manuscript submitted for publication.
- Weber K., A. D. Gvishiani, P. Gauderois, A. I. Gorshkov, A. F. Kushnir, V. F. Pisarenko, A. V. V. Trusov, M. L. Tsvang and S. L. Tsvang (1986). Classification of high-seismicity Zones in the Western Alps, *Izvestia, Earth Physics*, 22, 12, 965-976.

Presumed Explosions						
No	Date	Region	Lat.	Lon.	Mb	Ms
1	1985 02 10	East.Kaz. (5)	49.87	78.81	5.9	4.4
2	1984 12 28	East.Kaz. (5)	49.86	78.75	6.0	4.1
3	1988 09 14	East.Kaz. (5)	49.82	78.79	6.1	4.6
4	1988 11 12	East.Kaz. (5)	50.05	78.99	5.2	---
5	1988 11 23	East.Kaz. (5)	49.78	78.14	5.3	---
6	1985 04 25	East.Kaz. (5)	49.92	78.97	5.9	5.2
7	1987 02 26	East.Kaz. (5)	49.81	78.16	5.4	---
8	1987 03 12	East.Kaz. (5)	49.93	78.78	5.4	3.9
9	1987 04 03	East.Kaz. (5)	49.90	78.80	6.2	4.7
10	1987 04 17	East.Kaz. (5)	49.85	78.69	6.0	4.3
11	1987 04 19	Ural.Mount. (8)	60.78	57.50	4.5	---
12	1987 05 06	East.Kaz. (5)	49.77	78.09	5.5	---
13	1987 06 05	S.Sinkiang (6)	41.58	88.75	6.3	4.4
14	1987 06 06	East.Kaz. (5)	49.86	78.14	5.4	---
15	1987 07 06	Cent.Siberia (3)	61.49	112.78	5.2	---
16	1987 07 17	East.Kaz. (5)	49.78	78.12	5.8	4.5
17	1987 07 24	Cent.Siberia (3)	61.46	112.72	5.1	---
18	1987 08 02	East.Kaz. (5)	49.84	78.88	5.9	3.8
19	1987 08 02	N.Zemlya (1)	73.31	54.71	5.8	3.4
20	1987 08 12	Cent.Siberia (3)	61.42	112.71	5.0	---
21	1987 10 03	West.Kaz. (4)	47.63	56.21	5.2	---
22	1987 10 16	East.Kaz. (5)	49.78	78.24	4.6	---
23	1987 11 15	East.Kaz. (5)	49.87	78.79	6.0	4.8
24	1987 12 13	East.Kaz. (5)	49.95	78.85	6.1	4.5
25	1987 12 20	East.Kaz. (5)	49.75	78.02	4.8	---
26	1987 12 27	East.Kaz. (5)	49.83	78.74	6.1	4.5
27	1988 02 06	East.Kaz. (5)	49.86	77.96	4.8	---
28	1988 02 13	East.Kaz. (5)	49.92	78.90	6.0	4.5
29	1988 04 03	East.Kaz. (5)	49.88	78.96	5.9	---
30	1988 05 04	East.Kaz. (5)	49.91	78.72	6.2	---
31	1988 05 07	N.Zemlya (1)	73.35	54.26	5.5	3.8
32	1988 08 22	West.Siberia (2)	66.28	78.55	5.3	---
33	1988 06 14	East.Kaz. (5)	50.02	78.98	4.9	4.1
34	1988 09 29	S.Sinkiang (6)	41.82	88.25	4.8	---
35	1988 10 18	East.Kaz. (5)	49.86	78.12	4.9	---
36	1988 12 04	N.Zemlya (1)	73.36	55.07	5.9	---
37	1988 12 17	East.Kaz. (5)	49.88	78.92	5.9	4.5
38	1989 01 22	East.Kaz. (5)	49.91	78.86	6.0	4.5
39	1989 02 12	East.Kaz. (5)	49.89	78.75	5.9	4.4
40	1989 02 17	East.Kaz. (5)	49.87	78.12	5.0	---
41	1985 06 30	East.Kaz. (5)	49.86	78.69	6.0	4.2
42	1985 07 11	East.Kaz. (5)	49.90	78.80	3.5	---
43	1985 07 18	West.Russia (7)	65.97	40.86	5.0	3.7
44	1985 07 25	East.Kaz. (5)	49.89	78.15	5.0	4.0

**Table 2.2.1.** Listing of the presumed underground nuclear explosions recorded at NOR-ESS and used in our analysis. The region numbers (in brackets) refer to the specific USSR test sites shown in Fig. 2.2.1. The focal parameters are taken from the PDE and ISC bulletins. Note that Lat. and Lon. refer to latitude (degrees North) and longitude (degrees East), respectively. Note, Event 11 (Ural Mountains) is the second explosion on 19 April with origin time at 04.04.55.6.



## Presumed Earthquakes

No	Date	Lat.	Lon.	Depth	Mb	Ms
1	1984 11 02	42.00	84.06	33	4.5	---
2	1985 04 16	42.26	82.24	33(3)	4.5	---
3	1986 05 30	43.23	87.82	33	4.6	---
4	1986 06 12	43.67	87.33	33	4.8	---
5	1986 07 03	43.91	84.69	33	4.4	---
6	1986 07 17	43.32	77.85	33	4.5	---
7	1986 07 21	44.66	79.50	33	4.6	---
8	1986 07 24	43.79	87.25	33	4.5	---
9	1986 10 04	42.39	84.63	33	4.0	---
10	1986 11 20	42.04	84.39	50	4.6	---
11	1986 12 14	47.31	83.31	33	5.0	---
12	1987 04 04	42.45	79.95	33	4.1	4.1
13	1987 05 10	44.28	79.74	33	4.5	---
14	1987 05 26	42.92	78.06	20	4.6	---
15	1987 08 22	43.81	85.29	58	4.4	---
16	1987 09 18	47.01	89.65	33	5.3	4.8
17	1987 09 20	42.91	77.61	41	4.6	4.2
18	1987 10 06	43.43	88.54	32	4.8	4.0
19	1987 10 16	44.20	82.84	56	4.7	---
20	1988 02 08	43.73	83.76	10	4.3	---
21	1988 03 13	42.18	75.44	33	4.5	---
22	1988 03 15	42.21	75.50	33	4.5	---
23	1988 03 25	44.70	79.60	33	4.5	---
24	1988 05 25	42.01	85.69	22	5.2	---
25	1988 06 17	42.97	77.50	24	5.3	5.3
26	1988 09 27	46.80	73.59	5	4.3	---
27	1988 11 15	42.01	89.29	33	5.0	4.3
28	1989 03 05	42.51	74.63	33	5.3	4.1
29	1989 05 08	44.83	79.92	33	4.7	---
30	1985 02 03	42.06	84.34	-	4.5	---
31	1985 03 24	42.06	77.62	3	4.3	---
32	1985 06 02	43.80	85.65	21(45)	4.9	4.2
33	1985 07 16	42.22	82.36	45(22)	4.9	4.2
34	1985 08 14	42.13	82.44	33	4.1	---
35	1985 08 23	42.65	74.50	3	4.3	---

**Table 2.2.2.** Listing of presumed earthquakes recorded at NORESS and used in analysis. Epicenter locations are shown in the insert in Fig. 2.2.1. Caption otherwise as for Table 2.2.1.

## DISCRIMINATION RESULTS

Case	Data	Populations	Class. errors Reclass. J.knife	Class. features	Misclass. events	Marginal events
1	BEAM	All events	7	9	All	NE:22,21,31,32, 34,43; EQ:7,12,32; NE:11; EQ:16,17,29;
2	BEAM	All events	3	7	1,19,3,13	NE:22,19,31,32, 34,43; EQ:17; NE:36,42; EQ:7,25;
3	BEAM	All EQ Kazakh NE	1	3	19,13	NE:22; EQ:16,26; EQ:17;
4	OGF	All events	5	8	All	NE:18,19,32,34 42,43; EQ:11,26; NE:21; EQ:7,16,17;
5	OGF	All events	3	5	19,10,15, 13	NE:21,32,43 EQ:11,26 NE:19;
6	OGF	All EQ Kazakh NE	0	0	19,10	-- NE:25,30,42; EQ:7,26;

**Table 2.2.3.** Discrimination results for the Eurasian events listed in Tables 2.2.1 and 2.2.2, and recorded at the NORESS array. Classification features are extracted from ordinary beam (BEAM) traces and optimum group filtered (OGF) traces, where coherent noise has been suppressed. The explosion (NE) population was divided in two parts: all explosions or only those at the E. Kazakh test site (see Fig. 2.2.1). Classification (class.) errors are given for two cases: Reclassification where the event tested was part of the learning population and Jack-knife, where test event and learning population were independent. The "Reclass." results are always somewhat optimistic. Classification features are detailed in Figs. 2.2.3 and 2.2.6. Misclassified events and Marginal events refer to the numbering in Table 2.2.1 and 2.2.2. The most problematic event is EQ 26, that is, a presumed earthquake of 09/27/88 located at 46.8N, 73.6E (see Fig. 2.2.1), which also has a visual appearance of being an explosion. Waveforms for a representative number of events being either misclassified or rated marginal are shown in Fig. 2.2.8.

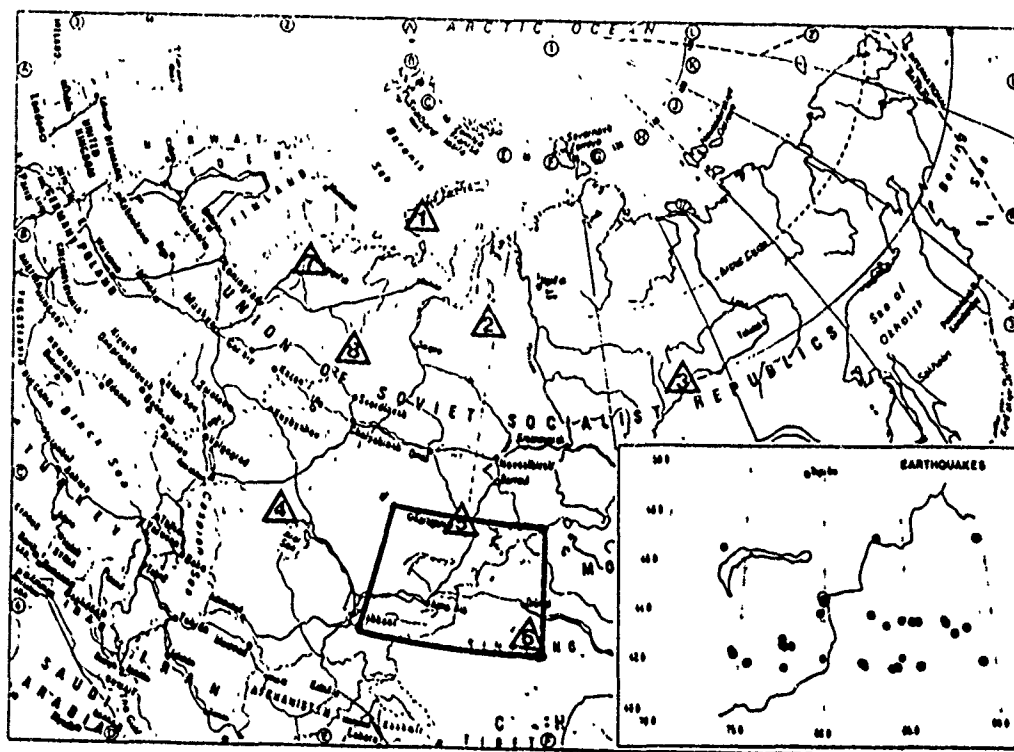


**Fig. 2.2.1.** Map outlining presumed explosion sites and presumed earthquake epicenters used in this classification study. The test sites are N. Zemlya (1); W. Siberia (2); Cent. Siberia (3); W. Kazakh (4); E. Kazakh (5); S. Sinkiang (6); W. Russia (7); and Ural Mountains (8). Focal parameter details in Tables 2.2.1 and 2.2.2.

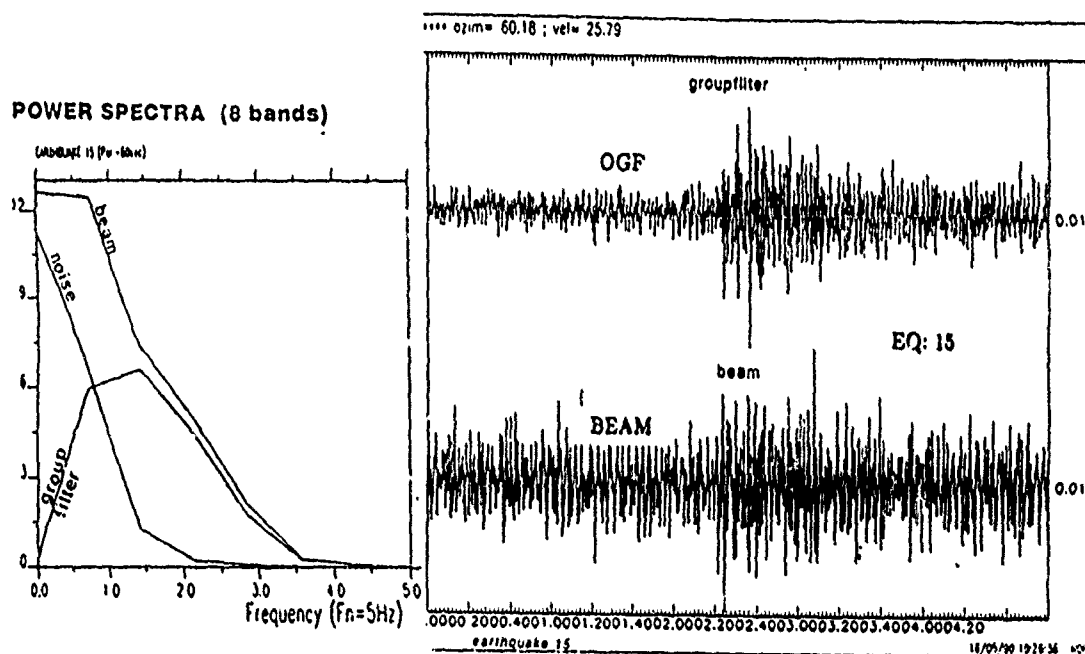
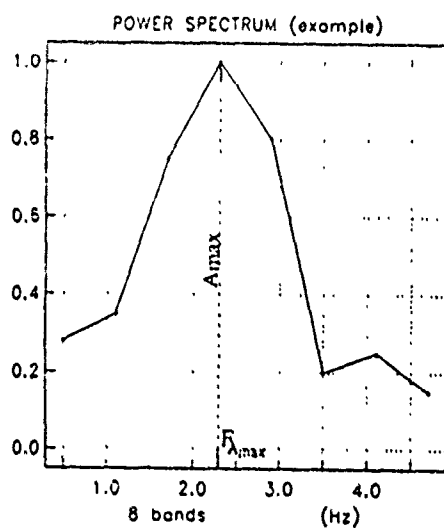


**Fig. 2.2.2.** Example of the relative efficiency of the Optimum Group Filtering (OGF) scheme of Kushnir et al (1990) relative to conventional array beamforming. The OGF filter suppresses most of the low frequency coherent noise as clearly seen in the figure to the left. The event analyzed here is an earthquake -- no. 15 in Table 2.2.2.

## PARAMETERS

P-phase (6 sec.)

parameters number	1	2	3	4	5	6	7	8
parameters value(Hz)	0.2-0.8	0.8-1.4	1.4-2.0	2.0-2.6	2.6-3.2	3.2-3.8	3.8-4.4	4.4-5.0



P-coda (30 sec.)

9	10	11	12	13	14	15	16
0.2-0.8	0.8-1.4	1.4-2.0	2.0-2.6	2.6-3.2	3.2-3.8	3.8-4.4	4.4-5.0

17	18	19
$F_{Amax}$ (P-phase)	$F_{Amax}$ (P-coda)	$Amax(P)/Amax(coda)$

**Fig. 2.2.3.** The 19 feature parameters used in this classification study. Center frequencies of the spectral bands used are shown to the left. Note, all spectral band values were normalized for each event with respect to  $A_{max}$ . In the calculation, the logarithmic feature values were used.

## P-spectra

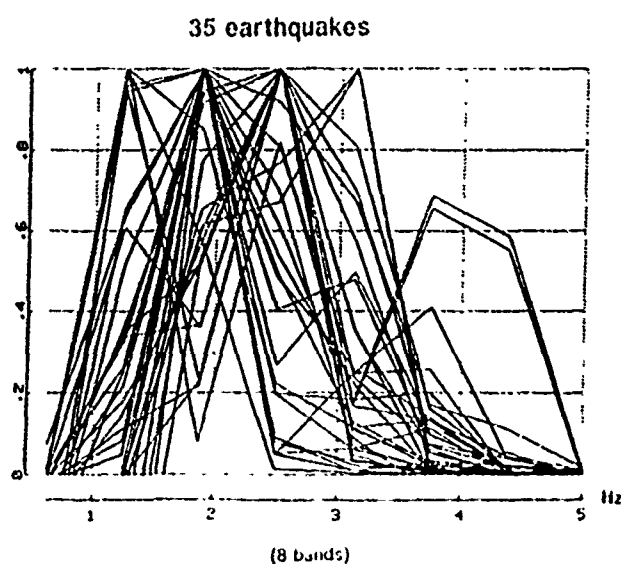
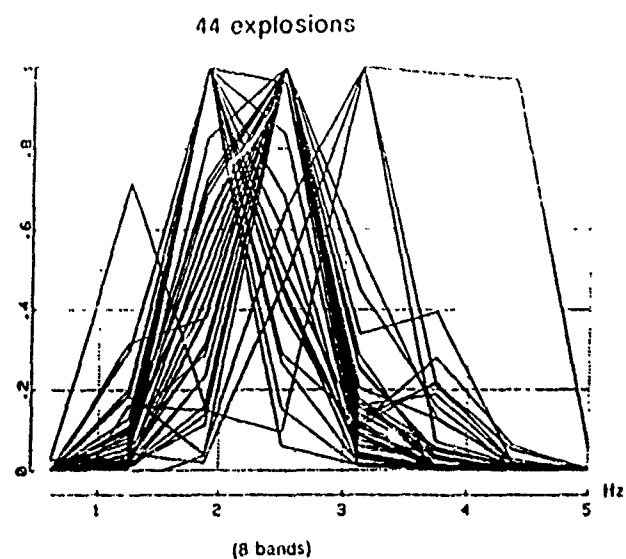


**Fig. 2.2.4.** Normalize power spectra (signal-noise) for all events used in analysis (Table 2.2.1 and 2.2.2). "Peaks" correspond to the center frequency of the eight spectral bands shown in Fig. 2.2.2. Seemingly, the largest spectral differences between the explosion and earthquake populations are in the range 0.5 - 1.5 Hz.

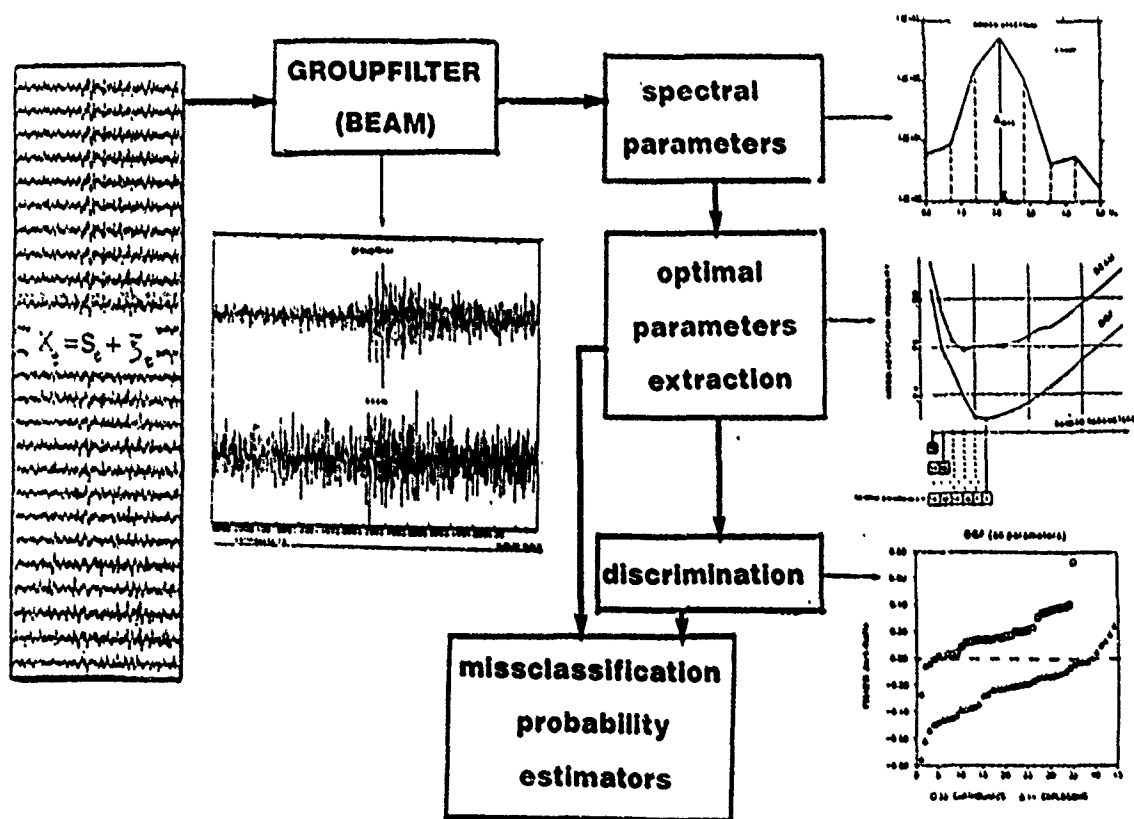
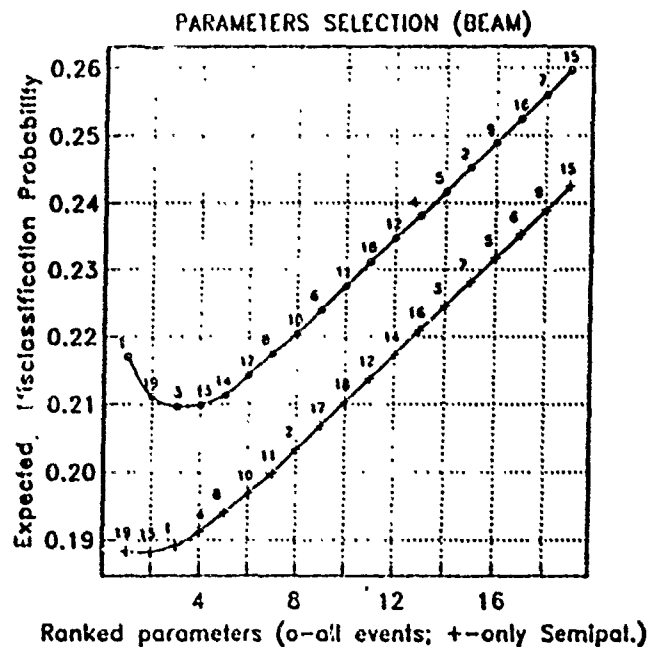
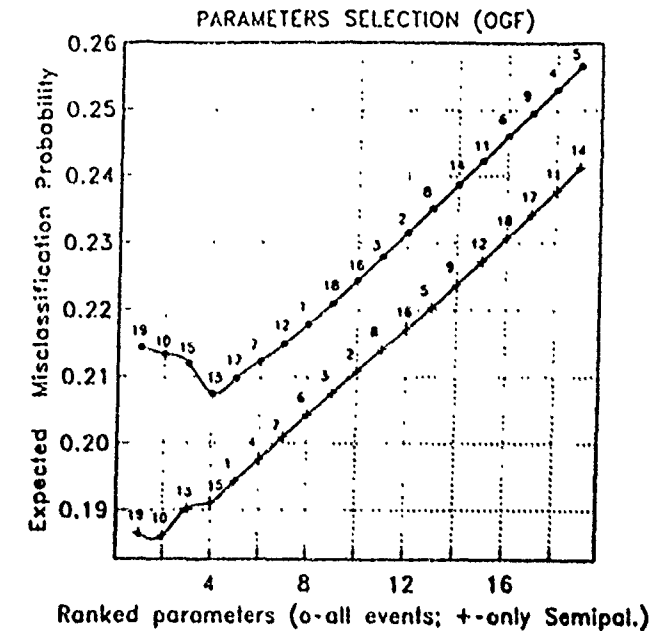


Fig. 2.2.5. Schematic illustration of the event classification procedure used. Further details in the text.



**Fig. 2.2.6.** The relative performance of feature parameters and combinations hereof as a function of the Expected Probability of Misclassification (EPMC) as defined in the text. OGF refers to optimum group filtered traces (removal of coherent noise), while BEAM refers to ordinary beam traces. Also, the upper curves refer to all events, while the lower ones refer to the subset of the Semipalatinsk or E. Kazakh test site explosions (Fig. 2.2.1). The minimum in the EPMC parameter implies that a combination of 2 or 4 classification features is optimum, as inclusion of additional feature parameters actually decreases the performance as discussed in the text.



## BEAM DISCRIMINATION

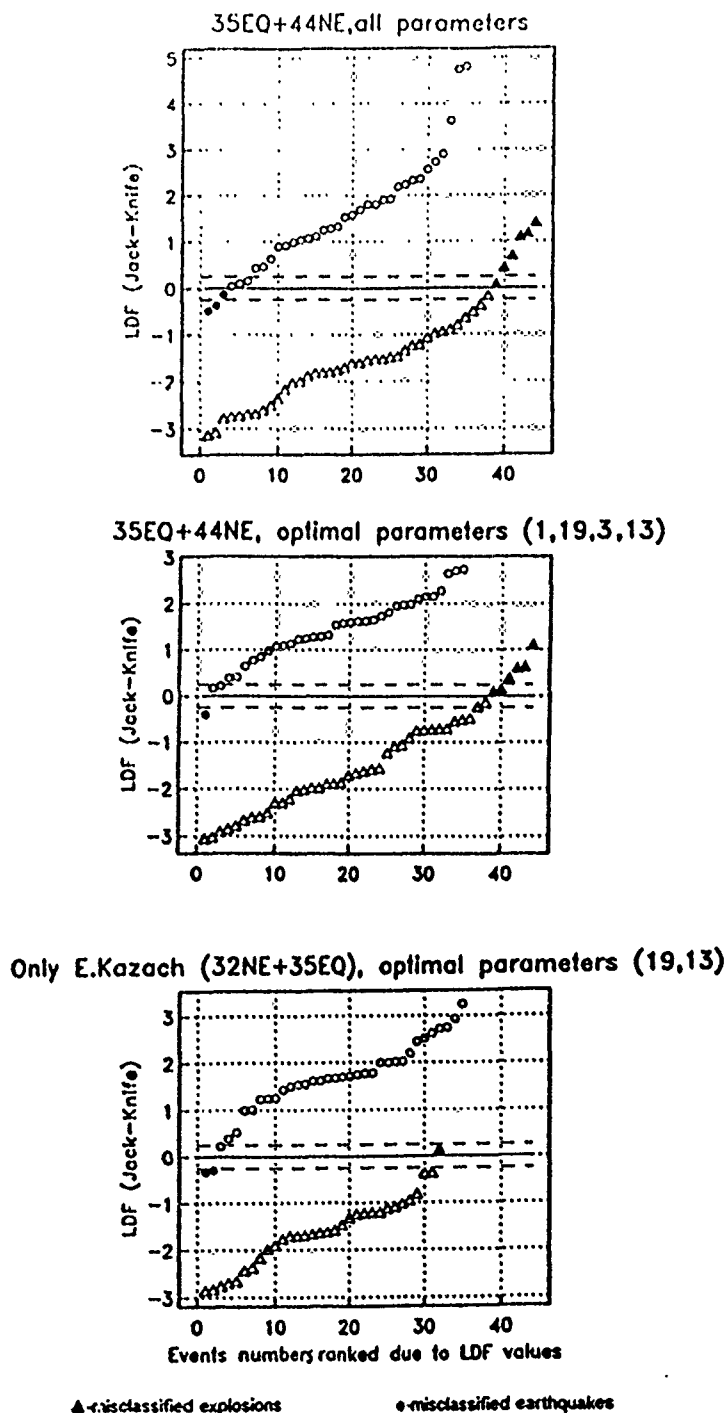


**Fig. 2.2.7a.** Event discrimination with feature parameters extracted from the conventional beam traces. The LDF (linear discrimination function) is defined in the text and Jack-Knife refers to the specific way of testing individual events independently against the learning population. The events are ranked relative to their LDF values, and thus not the way done in Tables 2.2.1 and 2.2.2. Events with LDF values within  $\pm 0.2$  units (stippled lines) are somewhat arbitrarily defined as marginal events. The 3 combinations of event populations and optimum parameter combinations coincide with Case 1-3 in Table 2.2.3.

## OGF DISCRIMINATION

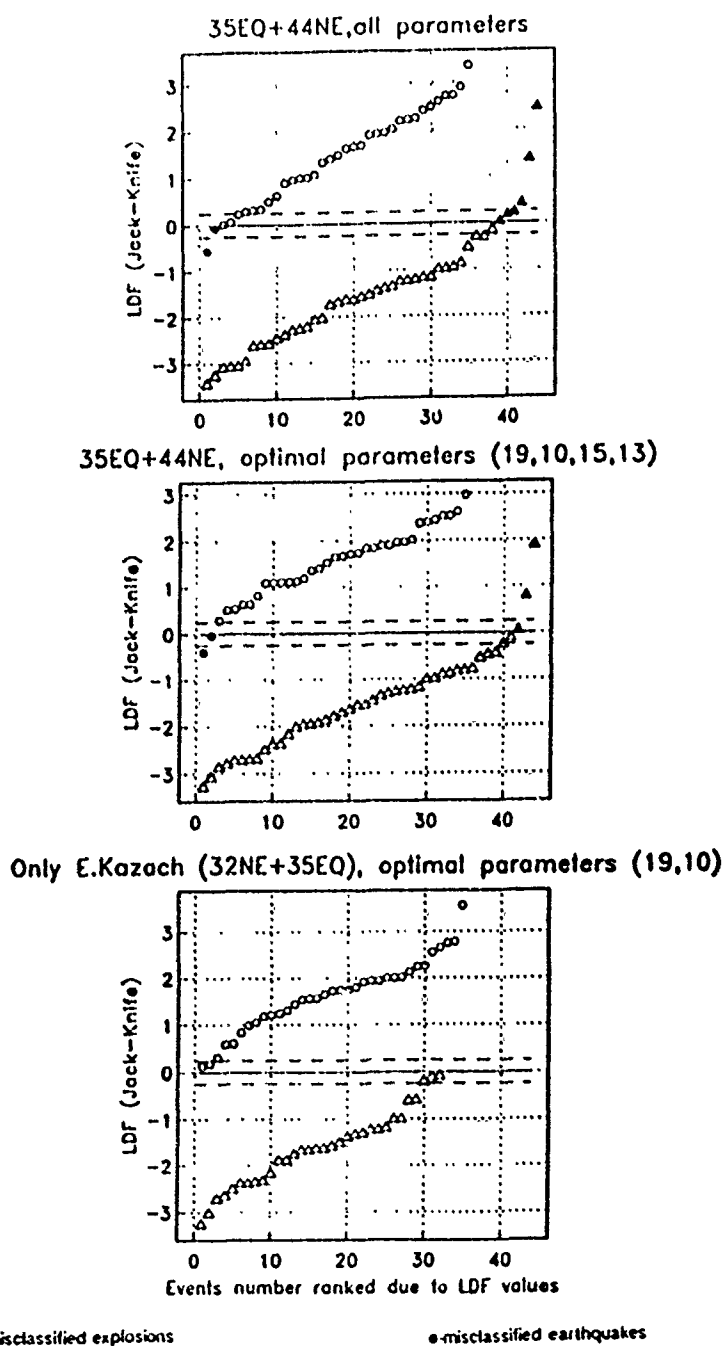


**Fig. 2.2.7b.** Event discrimination with feature parameters extracted from the OGF traces (optimum group filtered). Caption otherwise as for Fig. 2.2.7a.

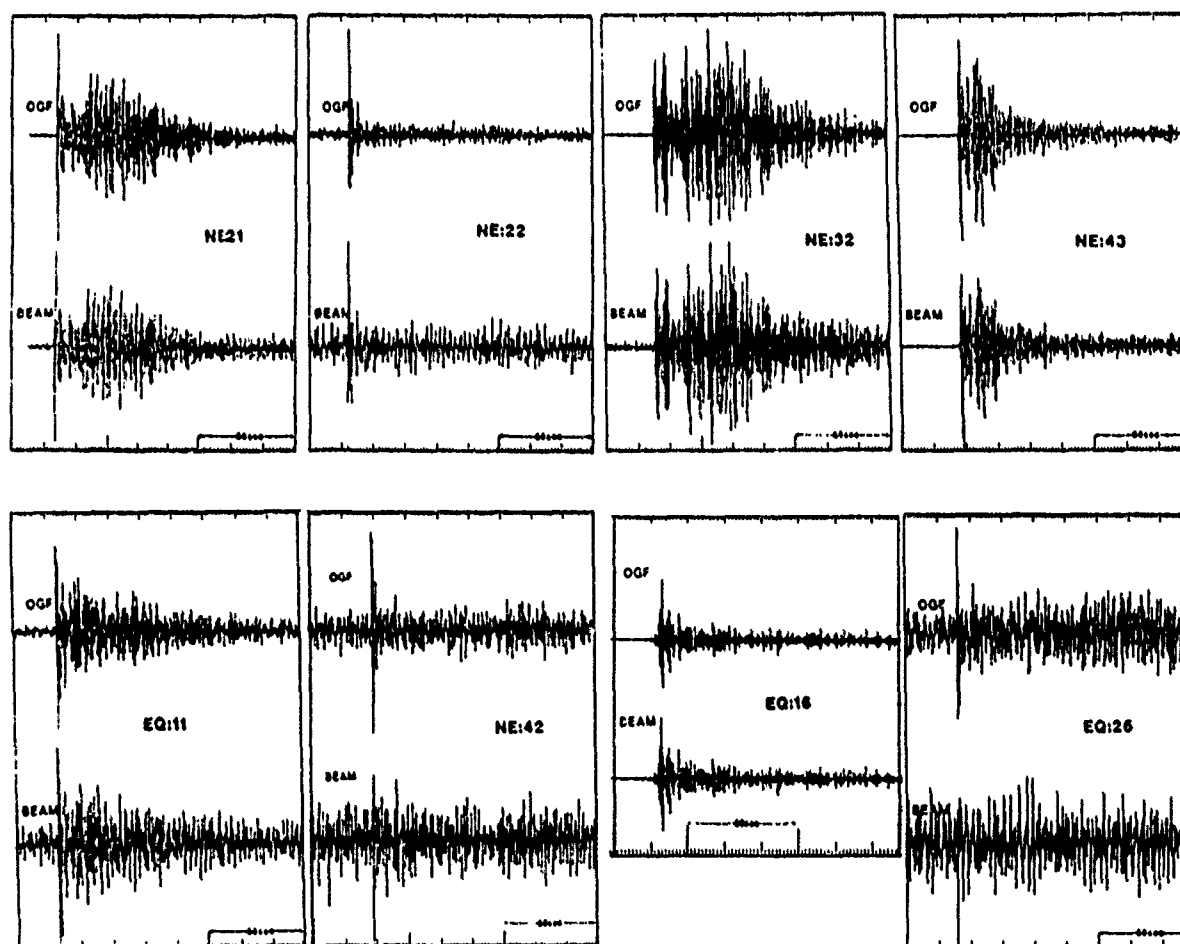


**Fig. 2.2.8.** Plot of OGF and conventional beam traces for misclassified and marginal events as listed in Table 2.2.3. The focal parameters of the EQ and NE events are shown. Most noticeable here is EQ26 which exhibits the basic feature of an explosion P wave.

## 2.3 Ray-based investigation of Lg azimuth anomalies at ARCESS

### *Introduction*

In a previous report (Bostock et al, 1990) we have discussed the application of the ray tracing technique of Bostock and Kennett (1990) to the characterization of Lg propagation to the NORESS array. We have considered the application of the same approach of representing the major features of the Lg phase via constructively interfering S waves multiply reflected within the earth's crust to understanding the azimuth anomalies observed at the ARCESS array.

### *Lg azimuth anomalies observed at ARCESS*

Figure 2.3.1 summarizes the Lg azimuth anomalies at ARCESS reported during the first eight weeks of operation of the IMS array analysis system in October and November 1989. The anomalies are also given in Table 2.3.1. The azimuth anomalies are plotted centered at the source point scaled by relative size with circles representing negative anomalies and triangles positive azimuth anomalies. The position of the ARCESS array is indicated by the filled triangle. The pattern of azimuth anomalies in Fig. 2.3.1 shows rapid changes in both the size and sign of the anomalies with geographic position. There is, however, a general trend for the anomaly to be negative for events along the Gulf of Estonia and more positive for events north of Leningrad.

### *Scandinavian crustal model and ray analysis*

Most models of the crustal thickness under Fennoscandia show a considerable depression of the Moho under the southern part of Finland and this would be expected to have a significant influence on the propagation of guided waves within the crust. The paths from sources in the Gulf of Estonia pass close to this feature and the predicted propagation patterns depend quite strongly on the detailed shape of the Moho.

For consistency with the earlier work we have retained the same model of the Moho structure under the Fennoscandian region (Fig. 2.3.2) and combined this with a smoothed version of the surface topography. We simplify the crustal model to a single layer with constant velocity with boundaries defined by the smoothed topography and Moho variations. For each source position we consider shooting a spray of rays, with a fixed phase velocity at the source, and then track the propagation of these rays through the structure. A convenient representation of the propagation process is provided by mapping the successive points of multiple reflection on the Moho boundary. For a waveguide of constant thickness these reflection points would be arcs of circles, and for a complex three-dimensional structure, the geometrical patterns of reflection points provide a useful measure of the distortion of the wavefronts spreading from the source.

We have found that shooting rays with an initial phase velocity of 4.0 km/s gives a good measure of the propagation process for Lg in our highly simplified model. It would be possible to take the effects of sedimentary structures near the surface into account by more complex ray tracing, but little additional physical insight would thereby be obtained. In

Fig. 2.3.3, we display the ray propagation patterns for three source locations representative of the clusters of events represented in the observed anomaly patterns of Fig. 2.3.1.

For a source in the Gulf of Estonia (A in Fig. 2.3.1), Fig. 2.3.3a displays the pattern of multiple reflections. The presence of the depression in the Moho surface has the effect of diverting energy towards the west and also of modifying the paths towards the ARCESS array which is marked by a triangle. The ray pattern varies significantly as the source position is moved along the Gulf of Estonia, and it is likely that the large variation in observed azimuths from this region is influenced by the interaction of the Lg phase with the complex Moho structure in southern Finland.

For a source to the north of Leningrad (B in Fig. 2.3.1), as shown in Fig. 2.3.3b, the influence of the Moho depression is more subtle. There is a tendency for ray paths to be drawn towards the depression because of the influence of the gradients at the Moho. The result is a degree of defocusing of energy travelling in the general direction of ARCESS. Once again the propagation patterns depend strongly on the precise location of the source relative to the Moho depression which has no topographic expression. The ray diagrams vary significantly for source displacements of the order of a tenth of a degree which again is consistent with the complexity of the observations from this area.

A more northerly source (C in Fig. 2.3.1), as illustrated in Fig. 2.3.3c, shows a more regular pattern of ray propagation, but we note that the Moho topography in northern Finland has led to a disruption of the reflected wavefront in the vicinity of the ARCESS array.

### *Discussion*

The azimuth anomalies calculated from this simple ray tracing scheme are given in Table 2.3.2 and are seen to be generally consistent with the trends in the observed anomalies displayed in Fig. 2.3.1. However, the ray picture for Lg is probably more valuable for providing a tool to investigate the sensitivity of guided wave propagation to the relative position of the source and major subsurface features such as the significant Moho topography under Finland.

**B.L.N. Kennett, M.G. Bostock, Research School of Earth Sciences,  
Australian National University  
S. Mykkeltveit**

*References*

- Bannister, S.C., B.O. Ruud and E.S. Husebye (1991): Tomographic estimates of sub-Moho seismic velocities in Fennoscandia and structural implications, *Tectonophysics*, 189, 37-53.
- Bostock, M.G. and B.L.N. Kennett (1990): Lg propagation patterns in three-dimensional heterogeneity, *Geophys. J. Intl.*, 101, 355-365.
- Bostock, M.G., B.L.N. Kennett and S. Mykkeltveit (1990): Ray-based interpretation of Lg azimuth anomalies at NORESS. *In: NORSAR Scientific Rep. No. 2-89/90, Semianual Tech. Summ.*, 1 October 1989 - 31 March 1990, Kjeller, Norway

---

Lat ( $^{\circ}$ N)	Lon ( $^{\circ}$ E)	$\Delta$ Azim
59.4	26.9	-10.0 $^{\circ}$
59.4	27.1	-19.4 $^{\circ}$
59.3	27.5	-18.2 $^{\circ}$
59.7	26.4	-3.0 $^{\circ}$
59.5	27.1	-19.4 $^{\circ}$
59.4	25.2	-5.2 $^{\circ}$
59.2	28.1	3.5 $^{\circ}$
60.9	29.3	5.8 $^{\circ}$
60.9	29.9	0.0 $^{\circ}$
60.6	29.2	-1.4 $^{\circ}$
61.9	31.1	6.7 $^{\circ}$
61.6	31.5	17.0 $^{\circ}$
61.4	35.0	-4.0 $^{\circ}$
61.9	36.3	-3.4 $^{\circ}$
61.4	35.5	0.9 $^{\circ}$
61.2	30.0	-0.3 $^{\circ}$
61.9	30.8	-3.1 $^{\circ}$
61.3	29.8	-4.1 $^{\circ}$
61.4	34.9	-1.6 $^{\circ}$
63.2	27.6	-9.1 $^{\circ}$
63.1	28.2	12.7 $^{\circ}$
63.0	35.0	-4.7 $^{\circ}$
64.0	23.5	0.8 $^{\circ}$
64.8	30.5	-18.0 $^{\circ}$
64.7	31.3	-9.4 $^{\circ}$
64.8	30.4	0.6 $^{\circ}$
64.8	30.7	-3.6 $^{\circ}$
65.7	25.5	-4.8 $^{\circ}$
65.7	17.1	-8.4 $^{\circ}$

---

**Table 2.3.1.** Lg azimuth anomalies at ARCESS from IMS analysis. The anomalies are relative to "true" azimuths based on event locations in the monthly bulletins issued by the University of Helsinki.

Source	Phase Vel.	Back Azim.	$\Delta$ Azim
A	3.8	175 <sup>0</sup> .14	-0.43 <sup>0</sup>
59.4 N	4.0		-1.40 <sup>0</sup>
27.1 E	4.2		-1.39 <sup>0</sup>
B	3.8	157 <sup>0</sup> .81	+3.75 <sup>0</sup>
61.6 N	4.0		+6.61 <sup>0</sup>
31.5 E	4.2		+7.99 <sup>0</sup>
C	3.8	151 <sup>0</sup> .54	-0.74 <sup>0</sup>
64.8 N	4.0		-0.73 <sup>0</sup>
30.5 E	4.2		+0.43 <sup>0</sup>

**Table 2.3.2.** Azimuth anomalies from ray tracing for sources at positions A, B and C (Fig. 2.3.1). These theoretical anomalies were computed for phase velocities of 3.8, 4.0 and 4.2 km/s. The sign of the theoretical anomalies corresponds to the same convention as the observed anomalies in Table 2.3.1.



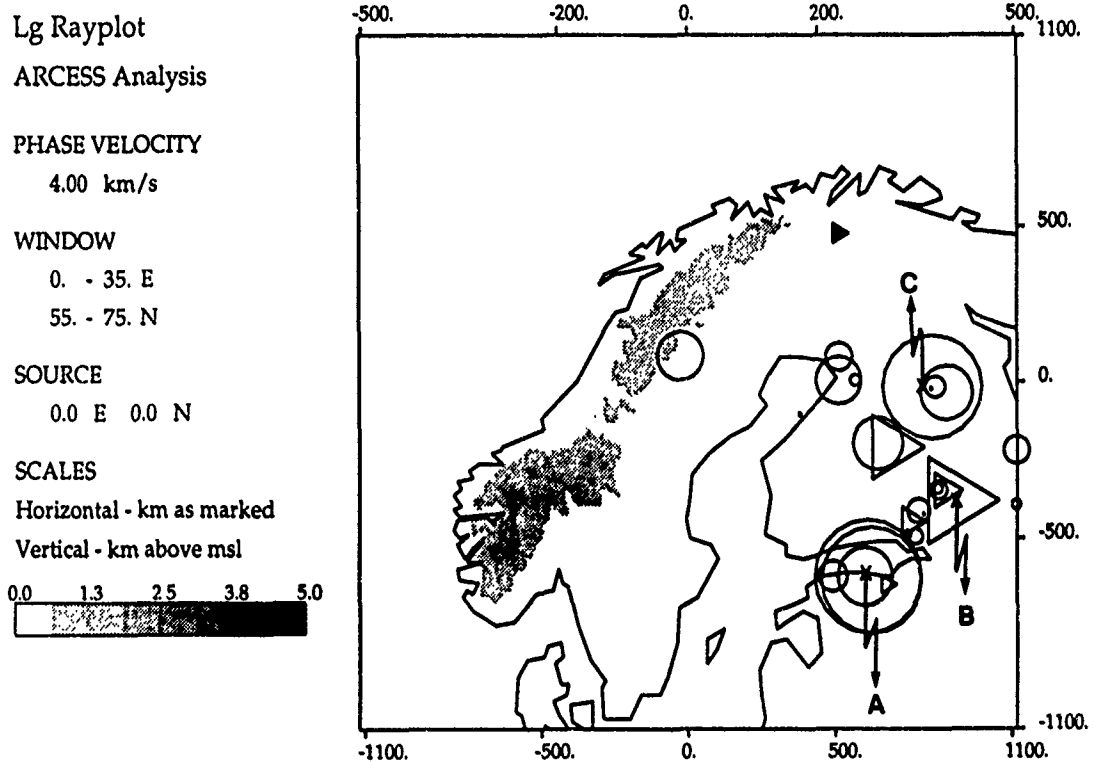


**Fig. 2.3.1.** The figure shows Lg azimuth anomalies at ARCESS reported during the first eight weeks of operation of IMS in October and November 1989. Circles represent negative values and triangles positive values of the anomalies. The position of ARCESS is indicated by a filled triangle. Also marked are the three source locations (A,B,C) used in the ray analysis in Fig. 2.3.3.

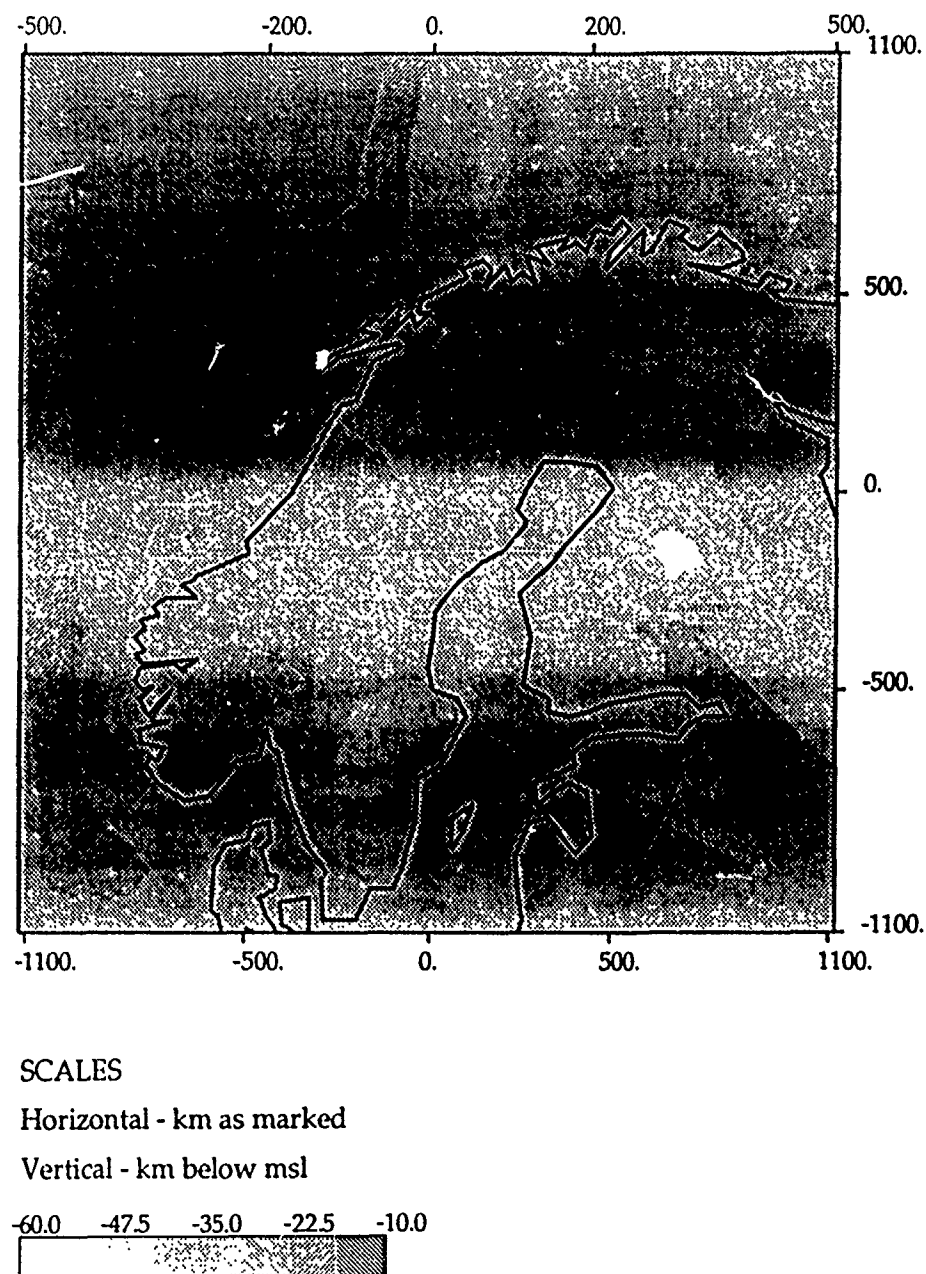


**Fig. 2.3.2.** Moho relief over Scandinavia, Finland and the Baltic states after Bannister et al (1991); lighter shades indicate increased Moho depths. The location of the ARCESS array is marked by a triangle.

## ARCESS Analysis

## PHASE VELOCITY

3.80 km/s

## WINDOW

0. - 35. E

55. - 75. N

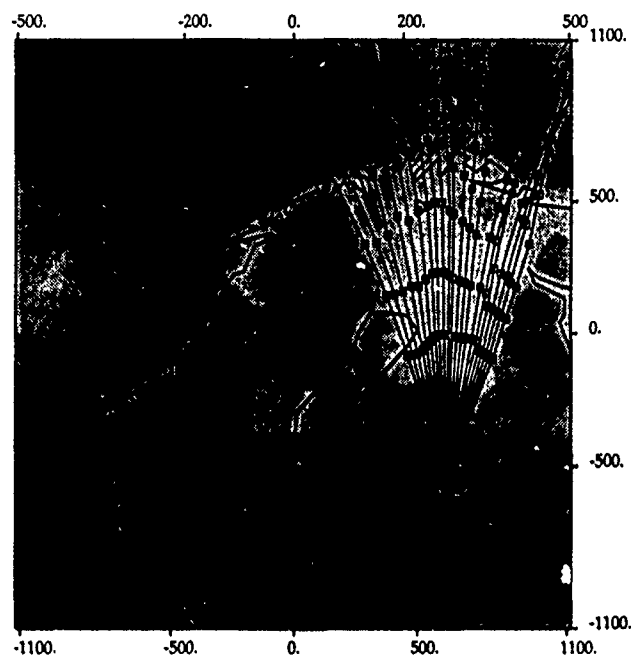
## SOURCE

27.1 E 59.4 N

## SCALES

Horizontal - km as marked

Vertical - km below msl



## ARCESS Analysis

## PHASE VELOCITY

4.00 km/s

## WINDOW

0. - 35. E

55. - 75. N

## SOURCE

27.1 E 59.4 N

## SCALES

Horizontal - km as marked

Vertical - km below msl

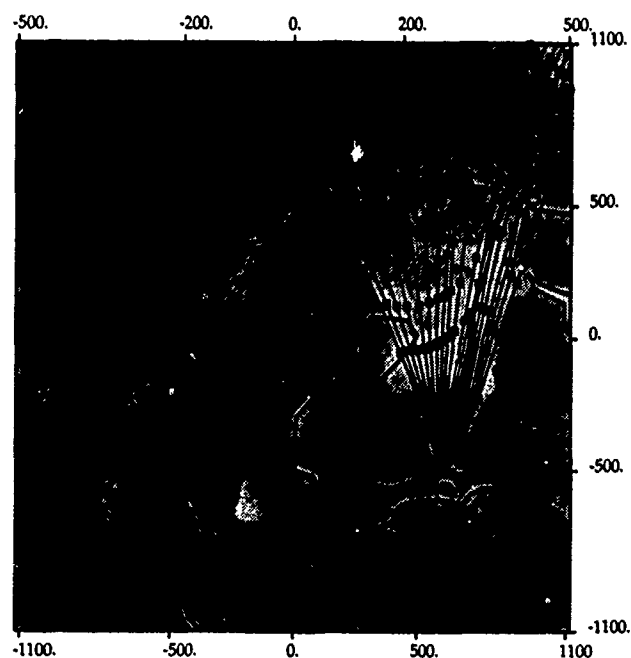
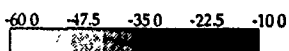


**Fig. 2.3.3a.** Ray diagrams for a source located at  $59.4^{\circ}\text{N}$ ,  $27.1^{\circ}\text{E}$  at phase velocities 3.8 km/s (top) and 4.0 km/s (bottom).

## ARCESS Analysis

## PHASE VELOCITY

3.80 km/s

## WINDOW

0. - 35. E

55. - 75. N

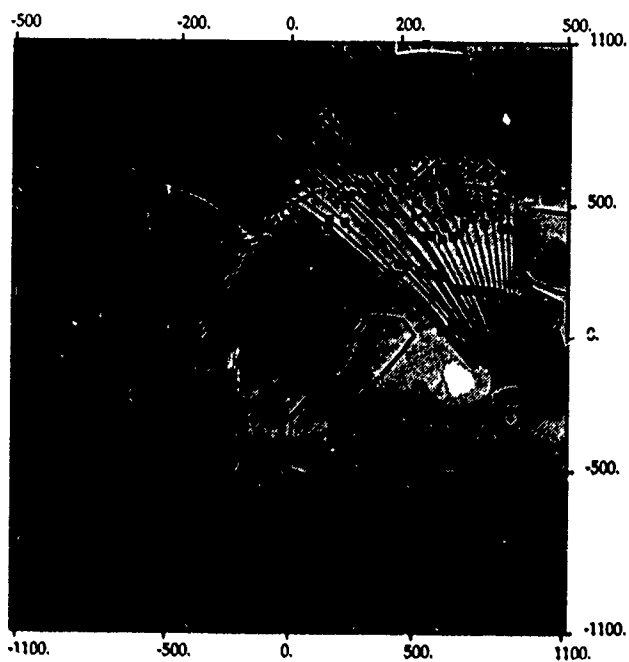
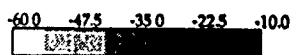
## SOURCE

31.5 E 61.6 N

## SCALES

Horizontal - km as marked

Vertical - km below msl



## ARCESS Analysis

## PHASE VELOCITY

4.00 km/s

## WINDOW

0. - 35. E

55. - 75. N

## SOURCE

31.5 E 61.6 N

## SCALES

Horizontal - km as marked

Vertical - km below msl

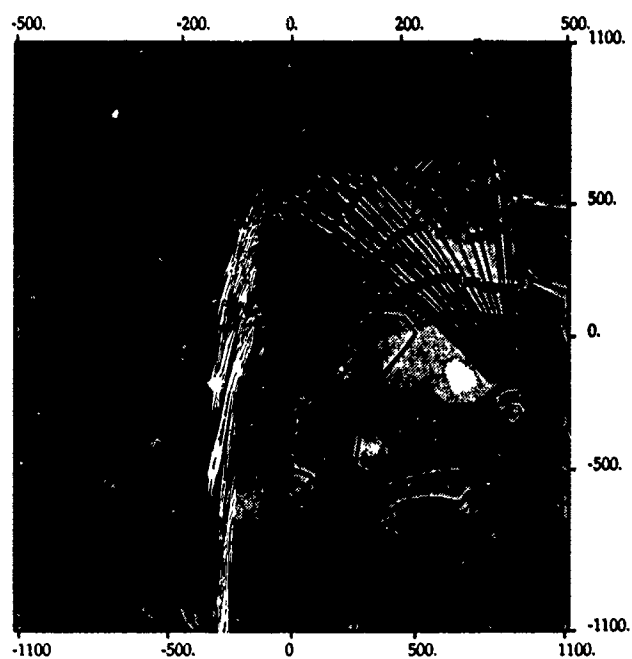


**Fig. 2.3.3b.** Ray diagrams for a source located at  $61.6^{\circ}\text{N}$ ,  $31.5^{\circ}\text{E}$  at phase velocities 3.8 km/s (top) and 4.0 km/s (bottom).

## ARCESS Analysis

## PHASE VELOCITY

3.80 km/s

## WINDOW

0. - 35. E

55. - 75. N

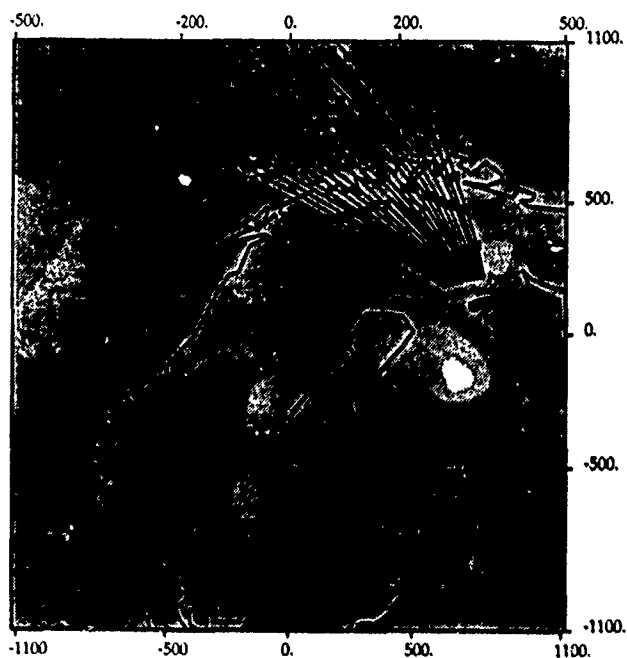
## SOURCE

30.5 E 64.8 N

## SCALES

Horizontal - km as marked

Vertical - km below msl



## ARCESS Analysis

## PHASE VELOCITY

4.00 km/s

## WINDOW

0. - 35. E

55. - 75. N

## SOURCE

30.5 E 64.8 N

## SCALES

Horizontal - km as marked

Vertical - km below msl

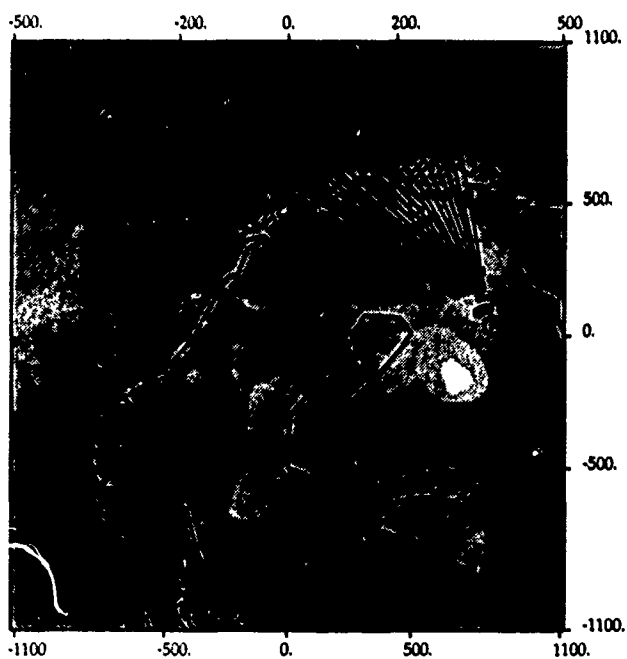


**Fig. 2.3.3c.** Ray diagrams for a source located at  $64.8^{\circ}\text{N}$ ,  $30.5^{\circ}\text{E}$  at phase velocities 3.8 km/s (top) and 4.0 km/s (bottom).

## 2.4 Lg as a yield estimation tool

### *Introduction*

The seismic Lg wave propagates in the continental lithosphere and can be observed from large explosions as far away as 5000 km in shield and stable platform areas (Nuttli, 1973; Baumgardt, 1985). Lg is generally considered to consist of a superposition of many higher-mode surface waves of group velocities near 3.5 km/s, and its radiation is therefore expected to be more isotropic than that of P waves. Thus, full azimuthal coverage is not essential for reliable determination of Lg magnitude. Furthermore, Lg is not affected by lateral heterogeneities in the upper mantle, which can produce strong focusing/defocusing effects on P-waves, and therefore contribute to a significant uncertainty in P-based  $m_b$  estimates.

In recent years, the Lg phase has emerged as maybe the most promising tool to obtain precise yield estimates by seismic means. The pioneering work by Otto Nuttli of Saint Louis University in the early 1970s first focused attention on using the Lg phase for seismic source size estimation, and Nuttli developed over the years a general technique for measuring Lg magnitude -  $m_b(Lg)$  - along any source-receiver path. He successfully applied this method to obtain excellent Lg-based yield estimates for NTS explosions, and also showed that the Lg phase could be used for teleseismic yield estimation at the main Soviet nuclear test sites.

Nuttli did his readings exclusively from analog seismograms, using a very sophisticated interactive analysis method. With the emergence of widespread digital recordings in the 1980s, the focus shifted to automatic digital processing, using in particular RMS measurements of digitally filtered traces (typically 0.6-3.0 Hz) in a fixed time window (typically 2 minutes). This method allowed reliable estimates to be made even at very low SNR, by using a noise compensation procedure. Assuming that independent yield estimates are available for calibration purposes, this method appears particularly well suited for TTBT monitoring of test sites of limited geographical extent.

Extensive research has been conducted by a number of scientists over the past decade investigating various aspects of Lg generation, propagation, attenuation and modelling. While recognizing the importance and impact of this work, it will lead too long to try to cover all of these topics in a brief review paper. I will therefore focus on the observational aspects of Lg as a tool for yield estimation. For a more extensive review of Lg related developments, reference is made to the paper by Hansen, Ringdøl and Richards (1990).

In this paper a review is given of the Lg magnitude estimation methodology, and of results obtained with regard to yield estimation. Results are briefly summarized for each of three test sites: Nevada, Semipalatinsk and Novaya Zemlya. The paper is concluded with a short discussion of the capabilities and limitation of Lg as a yield estimation tool. Some very recent results are included, in particular regarding the use of Lg for Novaya Zemlya explosions.

### *Lg results at NTS*

Much pioneering work on Lg waves was done in the 1970s and 1980s by Otto Nuttli of Saint Louis University. Thus, Nuttli (1973) proposed that "since Lg represents a higher-

mode wave traveling with minimum group velocity" it would be appropriate to relate amplitude ( $A$ ) and distance ( $\Delta$ ) via

$$A = K [\Delta^{-1/3}] [(\sin \Delta)^{-1/2}] e^{-\gamma \Delta} \quad (1)$$

where  $K$  is governed by the source strength, and  $\gamma$  is the coefficient of anelastic attenuation. The quality factor  $Q$  is related to  $\gamma$  by the equation:

$$\gamma = (\pi f) / (QU) \quad (2)$$

where  $U$  is the group velocity.

With the goal of defining a magnitude scale, based on  $L_g$  observations Nuttli described in detail (Nuttli 1973, 1986a) a three-step procedure to obtain what he called an  $m_b(L_g)$  value for an earthquake or an explosion of interest. The three steps were as follows:

- (i)  $\gamma$  was estimated for a particular source-receiver path;
- (ii) equation (1) was used to predict an amplitude at one particular distance (he chose  $\Delta$  corresponding to 10 km for reference); and
- (iii) magnitude was assigned via the formula

$$m_b(L_g) = 5.0 + \log [A(10 \text{ km}) / 110]$$

where  $A(10 \text{ km})$  is the amplitude, in microns, resulting from (ii).

For 22 nuclear explosions below the water table at NTS, Nuttli (1986a) showed that his  $m_b(L_g)$  values, using only three WWSSN stations in the western U.S., were remarkably well correlated with the logarithm of announced yield. He proposed a best-fitting line through this magnitude-yield data, from which magnitudes had a standard deviation of only about 0.05. Patton (1988) developed computer-automated measures of  $L_g$  amplitude aiming at reproducing Nuttli's NTS results (see Fig. 2.4.1). Patton measured  $L_g$  amplitudes from digital seismograms in two ways -- by using the third-largest peak and by computing the RMS amplitude in the  $L_g$  time window -- and found very little difference (around 0.01 magnitude unit) in the amount of scatter about regression lines using the two measures. However, he found that standard deviations from best-fitting  $m_b(L_g) / \log(\text{yield})$  relations were low, 0.07-0.08 magnitude units, only if explosions were restricted to sub-regions of NTS (Pahute Mesa, northern Yucca Flat, southern Yucca Flat).

### *Lg results at Semipalatinsk*

Based on the success in estimating yields for NTS explosions, Nuttli proceeded to apply the same magnitude-yield relation, together with  $L_g$  signals recorded at analog WWSSN stations in Eurasia, to estimate the yields of nuclear explosions at the main Soviet test site (Shagan River, Semipalatinsk) (Nuttli 1986b). For the period 1978-1984, after the 150 kt Threshold Test Ban Treaty had gone into effect, his yield estimates for Shagan River explosions included twenty that exceeded the threshold, including one (1982 December 5) estimated by Nuttli to be about 300 kt. While acknowledging the pioneering work involved in these studies, it is clear that the generally low signal-to-noise ratios and the problematic data quality of these analog recordings made very precise measurements impossible to attain, a fact also recognized by Nuttli himself. Also, at the teleseismic dis-

tances for which Nuttli had Lg data, 1900-4400 km, yield estimates based on absolute measures of ground motion that have to be extrapolated back to 10 km are a severe test of the validity of eq. (1), and, even if eq. (1) is appropriate, are very sensitive to errors in  $\gamma$  by 10-15% would result in yield estimates about two times too high.

In the first of a number of Lg studies undertaken by the NORSAR staff during the 1980s, Ringdal (1983) analyzed digital NORSAR Lg data of selected Semipalatinsk underground nuclear explosions. He found that when using NORSAR RMS Lg instead of P waves recorded at NORSAR to estimate source size, it was possible effectively to eliminate the magnitude bias relative to world-wide  $m_b$  observed at NORSAR between Degelen and Shagan River explosions. The method consisted of averaging log (RMS) values of individual NORSAR channels, filtered in a band 0.6-3.0 Hz in order to enhance Lg signal-to-noise ratio. Ringdal and Hokland (1987) expanded the data base, and introduced a noise compensation procedure to improve the reliability of measurement at low SNR values. They were able to identify a distinct P-Lg bias between the northeast and southwest portions of the Shagan River test site (see Fig. 2.4.2), a feature that was confirmed by Ringdal and Fyen (1988) using Graefenberg array data. Ringdal and Marshall (1989) combined P and Lg based source size estimators to estimate the yields of 96 Shagan River explosions during 1965-1988, using data on the cratering explosion 15 January 1965 as a reference for the yield calculations.

Hansen, Ringdal and Richards (1990) analyzed available data from stations in China and the Soviet Union, and found that RMS Lg of Semipalatinsk explosions measured at these stations showed excellent consistency (see Fig. 2.4.3). They concluded that for explosions at Semipalatinsk with good signal-to-noise ratio,  $m_b(Lg)$  may be estimated at single stations with an accuracy (one standard deviation) of about 0.03 magnitude unit. It is noteworthy that this high accuracy was consistently obtained for a variety of stations at very different azimuths and distances, even though the basic parameters remained exactly as originally proposed for NORSAR recordings (0.6-3.0 Hz bandpass filter, RMS window length of 2 minutes, centered at a time corresponding to a group velocity of 3.5 km/s).

A possibility to compare Lg and P magnitudes to published yields for Semipalatinsk explosions has recently emerged with the recent publication by Soviet scientists quoting yield estimates for a number of such explosion (Bocharov et al, 1989; see also Vergino, 1989a,b). Since these explosions were all conducted prior to 1973, there are very few available high-quality digital records of the events. Nevertheless, based on those NORSAR recordings that are available, the correspondence between log RMS Lg and log yield is excellent (Ringdal, 1990). A suite of analog recordings obtained from stations within the Soviet Union has recently been digitized and made available as part of bilateral US-USSR arrangements. Israelson (1991) has computed RMS Lg of these recordings and has found excellent correspondence with the yields published by Bocharov et al (1989).

#### *Lg results at Novaya Zemlya*

No yield data have so far been published from Soviet sources for explosions at the Novaya Zemlya test site. Thus an assessment of the Lg potential can only be made in an indirect way. Ringdal and Fyen (1991) compared NORSAR and Graefenberg RMS Lg for Novaya Zemlya explosions using the same procedure as earlier done for Semipalatinsk. Fig. 2.4.4 shows the propagation paths to the two arrays along with examples of recorded Novaya Zemlya explosions.



Fig. 2.4.5 shows the correspondence between RMS Lg at NORSAR and Grafenberg, and also compares various other source size estimators. Note that world-wide  $m_b$  corresponds extremely well with NORSAR P-coda magnitude, but correlates very poorly with either NORSAR or Grafenberg RMS Lg. Note also that the RMS Lg correspondence between Grafenberg and NORSAR is excellent, with an orthogonal standard deviation of only 0.035. The scatter is further reduced (to 0.025) if we consider only events with at least 5 available GRF channels (Ringdal and Fyen, 1991). Thus, we obtain the same close correspondence between Lg observations from these two arrays for Novaya Zemlya explosions as has previously been observed for Semipalatinsk events.

With the current lack of independently obtained calibration data, it would be premature to draw any firm conclusions as to the relative accuracy of RMS Lg in estimating yields of these explosions. Nevertheless, it would appear that the close grouping in RMS Lg, especially seen for the NORSAR data, is unlikely to be a coincidence. It would seem reasonable to conclude that this group of explosions has very nearly the same yield, in spite of the divergence in  $m_b$  estimates. However, additional analysis, in particular including available Lg data from Soviet stations for this event set, should be performed in order to further test this hypothesis. Initial results from processing data from Soviet stations seem to give some support in this regard (Israelson, 1991).

### *Discussion*

Most of the evidence for the "stability" of Lg magnitudes is indirect. By pairwise comparison of RMS Lg for a number of different source-receiver paths, it has been demonstrated that single-station RMS Lg can be used to estimate relative magnitude with a remarkably small scatter (0.02-0.03 in  $m_b$  units orthogonally). This was first shown for Semipalatinsk explosions, but has recently been confirmed also for explosions at Novaya Zemlya. The latter observation is particularly interesting, since many of the paths exhibited significant "Lg blockage" effects (Baumgardt, 1990). The Lg blockage is for example seen on NORSAR recordings, where the Lg phase is relatively weak compared to P and Sn.

NORSAR and Grafenberg array measurements of Lg waves from the Shagan River area have been demonstrated as being sufficiently precise to allow a systematic P-Lg magnitude bias to be identified between the NE and SW parts of that site. Available yield data from Soviet sources indicate that Lg magnitudes show better consistency with yield than does P-based magnitudes for explosions from this area. The reason for this P-Lg bias has been the subject of much discussion. The most likely explanation appears to be P-wave focusing/defocusing effects in the upper mantle underlying the source region.

A heuristic explanation for the apparently superior stability of Lg waves compared to P waves in measuring source size lies in the difference in the nature of the sampling of the seismic source for each of these phases. Teleseismic P waves sample only a very limited portion of the focal sphere, and are susceptible to strong focusing/defocusing effects in the upper mantle. Lg waves are composed of multiple rays that sample a larger portion of the focal sphere, and appear to have less significant focusing/defocusing effects along their propagation paths. In a sense, Lg waves "let the Earth do the averaging".

Still, there are many uncertainties remaining with regard to the potential of Lg as a yield estimator. The most significant question mark would appear to be the effects of full or par-

tial "Lg blockage". As noted above, such blockage does not seem to have much effect on RMS Lg stability if the blockage structure is well removed from the source region (cf. NORSAR Lg blockage for Novaya Zemlya explosions). This is reasonable since the blockage effects would in this case be similar for all the events.

However, a different situation arises if full or partial "Lg blockage" structures are located within or in the immediate neighborhood of the test site. It is easy to see that the stability of Lg would be severely affected in such cases. In this connection, it is noteworthy that RMS Lg at NTS does not seem to show the same "stability" as at the two Soviet test sites (Richards, personal communication). It would seem likely that such local partial "blockage" effects at NTS might account for this difference.

Lg waveforms cannot at present be modelled with the same quality of fit between synthetics and data that has been attained with other phases, and many aspects of Lg generation and propagation characteristics are still not well understood. Among topics that need further study are Lg blockage and scattering effects caused by tectonic heterogeneities and the effects of topography, near source geology and depth of burial on Lg excitation. Much challenging work therefore remains to be done in this field.

**F. Ringdal**

### *References*

- Baumgardt, D.R. (1985): Comparative analysis of teleseismic P coda and Lg waves from underground explosions in Eurasia, *Bull. Seism. Soc. Am.*, 75, 1413-1433.
- Baumgardt, D.R. (1990): Investigation of teleseismic Lg blockage and scattering using regional arrays, *Bull. Seism. Soc. Am.*, Special Issue, 80, 2261-2281.
- Bocharov, V.S., S.A. Zelentsov and V.I. Mikhailov (1980): Characteristics of 96 underground nuclear explosions at the Semipalatinsk test facility, *Atomic Energy*, 67, 3, 210-214 (in Russian).
- Hansen, R.A., F. Ringdal and P.G. Richards (1990): The stability of RMS Lg measurements, and their potential for accurate estimation of the yields of Soviet underground nuclear explosions, *Bull. Seism. Soc. Am.*, Special Issue, 80, 2106-2126.
- Israelson, H. (1991): Manuscript in preparation.
- Leith, W. (1987): Tectonics of eastern Kazakhstan and implications for seismic source studies in the Shagan River area. In: Papers presented at the 9th Annual DARPA/AFGL Seismic Research Symposium, 15-18 June 1987, 34-37.
- Nutli, O.W. (1973): Seismic wave attenuation and magnitude relations for eastern North America, *J. Geophys. Res.*, 78, 876-885.

- Nuttli, O.W. (1986a): Yield estimates of Nevada test site explosions for eastern North America, *J. Geophys. Res.*, 91, 2137-2151.
- Nuttli, O.W. (1986b): Lg magnitudes of selected East Kazakhstan underground explosions, *Bull. Seism. Soc. Am.*, 76, 1241-1251.
- Patton, H.J. (1988): Application of Nuttli's method to estimate yield of Nevada test site explosions recorded on Lawrence Livermore National Laboratory's digital seismic system, *Bull. Seism. Soc. Am.*, 78, 1759-1772.
- Ringdal, F. (1983): Magnitudes from P coda and Lg using NORSAR data, *In: NORSAR Semiann. tech. Summ.*, 1 Oct 1982 - 31 Mar 1983, NORSAR Sci. Rep. 2-82/83, Kjeller, Norway.
- Ringdal, F. (1990): Detection and yield estimation studies, *In: Semiann. Tech. Summ.*, 1 April - 30 September 1990, NORSAR Sci. Rep. 1-90/91, Kjeller, Norway.
- Ringdal, F. and B.Kr. Hokland (1987): Magnitudes of large Semipalatinsk explosions using P coda and Lg measurements at NORSAR, *In: Semiann. Tech. Summ.*, 1 Apr - 30 Sep 1987, NORSAR Sci. Rep. 1-87/88, Kjeller, Norway.
- Ringdal, F. and J. Fyen (1988): Comparative analysis of NORSAR and Grafenberg Lg magnitudes of Shagan River explosions, *In: Semiann. Tech. Summ.*, 1 Apr - 30 Sep 1988, NORSAR Sci. Rep. 1-88/89, Kjeller, Norway.
- Ringdal, F. and P.D. Marshall (1989): Yield determination of Soviet underground nuclear explosions at the Shagan River Test Site, *In: Semiann. Tech. Summ.*, 1 Oct 1988 - 31 Mar 1989, NORSAR Sci. Rep. No. 2-88/89, Kjeller, Norway.
- Ringdal, F. and J. Fyen (1991): RMS Lg analysis Novaya Zemlya explosion recordings, *In: Semiann. Tech. Summ.*, 1 Oct 1990 - 31 Mar 1991, NORSAR Sci. Rep. No. 2-90/91, Kjeller, Norway.
- Vergino, E.S. (1989a): Soviet test yields, *EOS, Trans. Am. Geophys. Un.*, 1511+, November 28.
- Vergino, E.S. (1989b): Soviet test yields, Corrections and Additions, *EOS, Trans. Am. Geophys. Un.*, 1569, December 26.

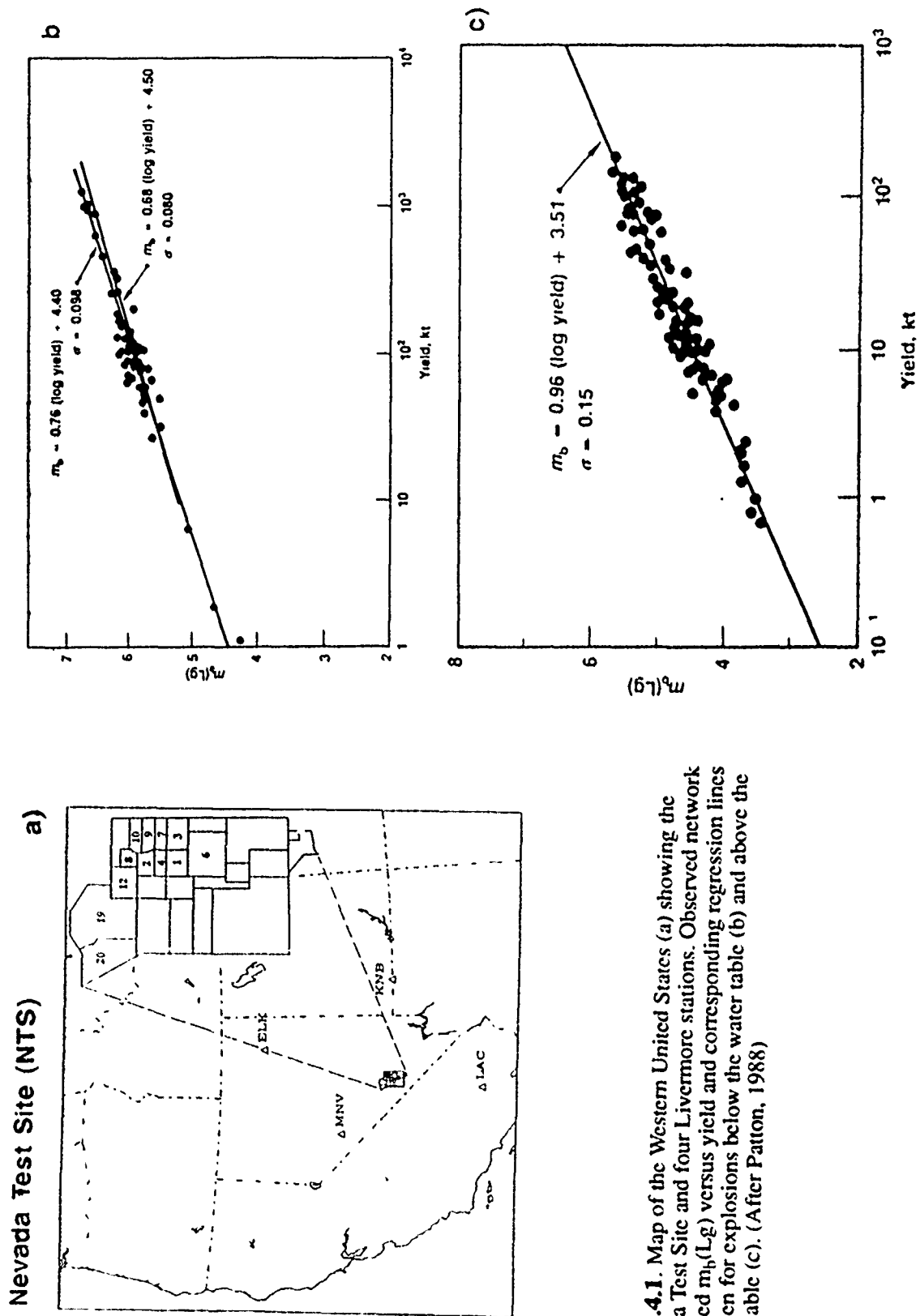


**Fig. 2.4.1.** Map of the Western United States (a) showing the Nevada Test Site and four Livermore stations. Observed network averaged  $m_b(Lg)$  versus yield and corresponding regression lines are given for explosions below the water table (b) and above the water table (c). (After Patton, 1988)

# Shagan River Test Site, USSR

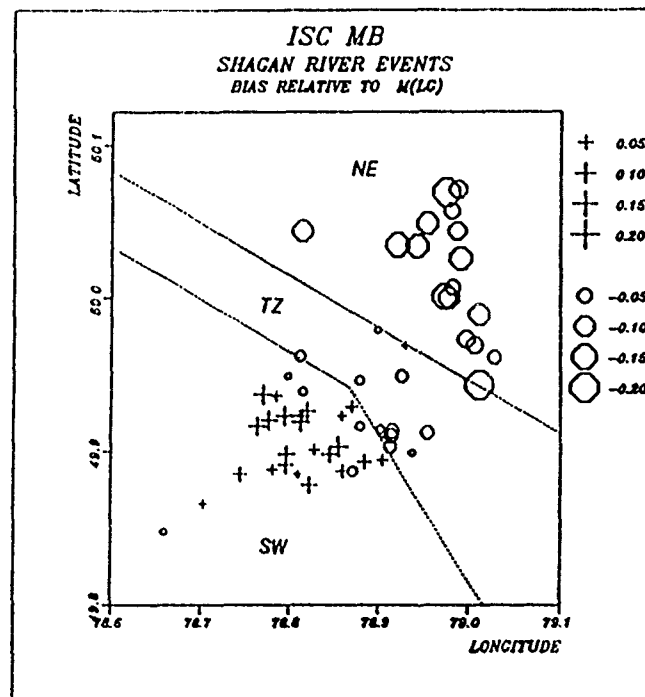
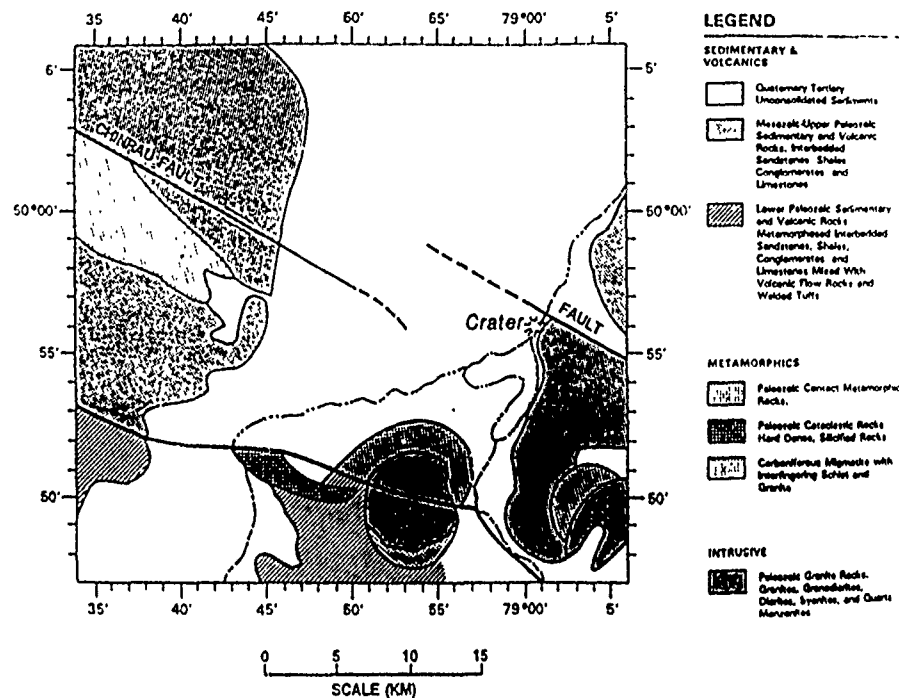


**Fig. 2.4.2.** Map of the Shagan River area (top), showing the surface geology (see Leith, 1987). The bottom figure illustrates the systematic P-Lg magnitude bias across the test site, and the correction with the observed faults. (After Ringdal and Marshall, 1989.)

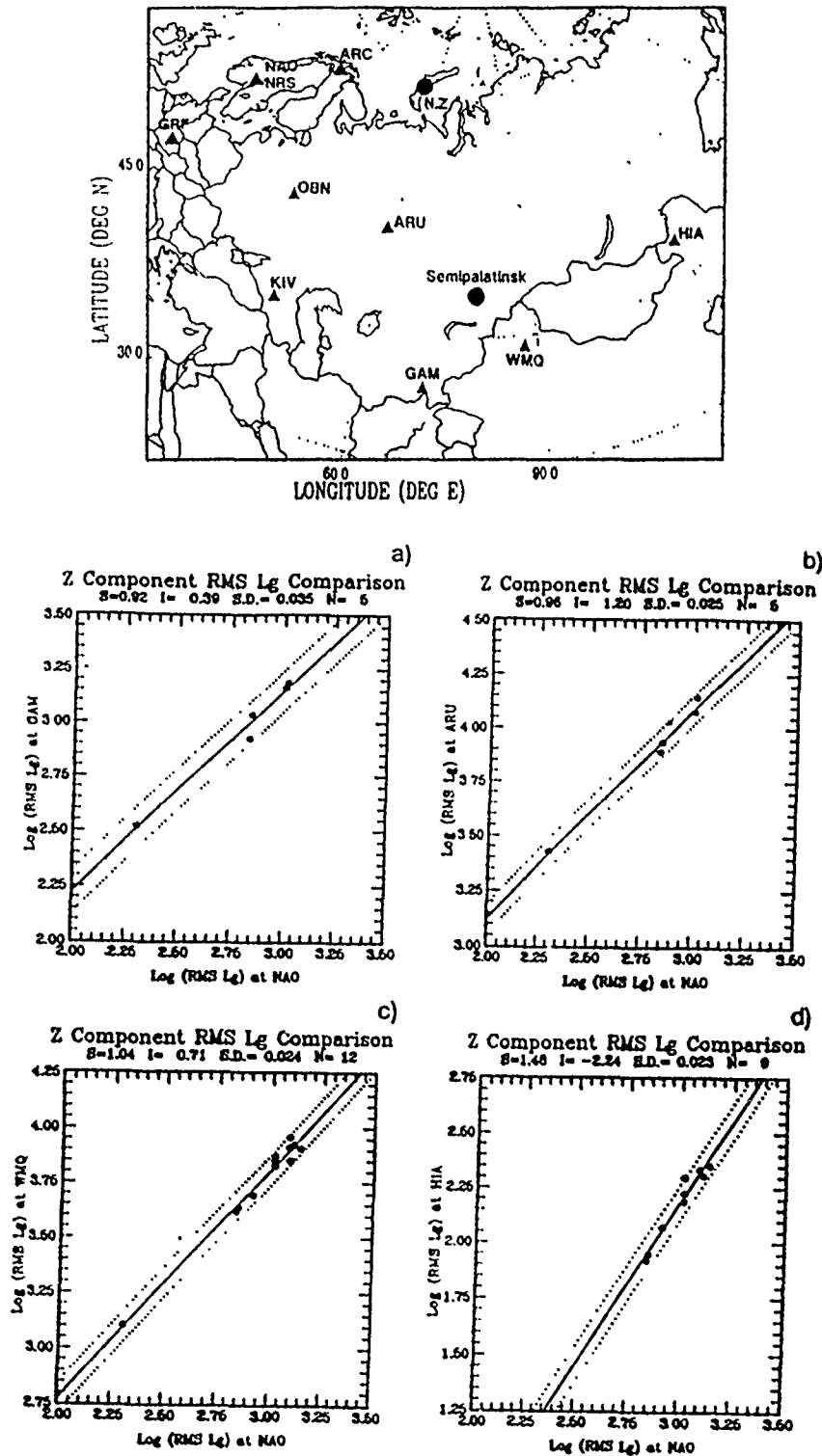


**Fig. 2.4.3.** The map at the top shows the location of stations analyzed in the study by Hansen, Ringdal and Richards (1990) (triangles) relative to the two main Soviet test sites. The bottom part, figures a)-d), shows the excellent RMS Lg correspondence between four of the stations in the USSR/China and the NORSAR array for Shagan River explosions.

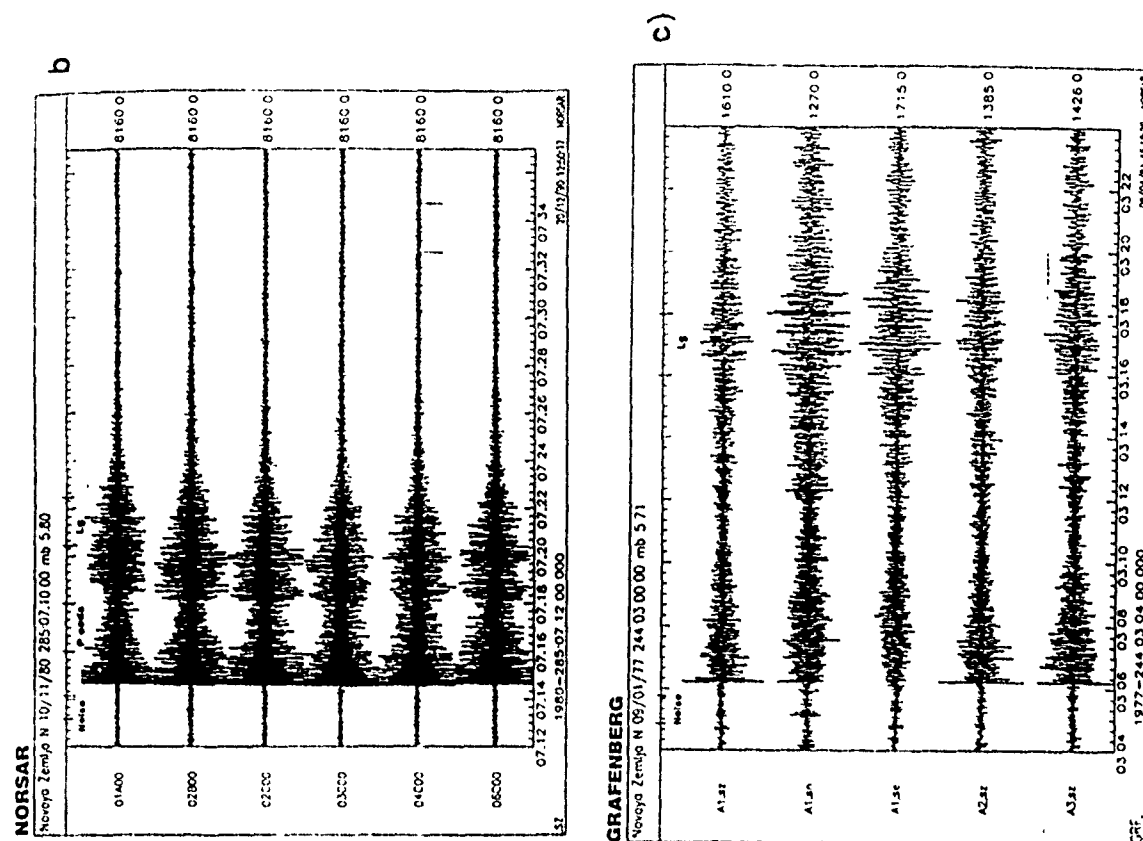


**Fig. 2.4.4.** a) Map showing the Lg propagation paths from the main Soviet test sites (Novaya Zemlya and Semipalatinsk) to the NOR SAR and Grafenberg arrays. Typical recordings of explosions from Novaya Zemlya are shown for NOR SAR (b) and Grafenberg (c). (After Ringdal and Fygn, 1991)

### RMS Lg Novaya Zemlya - NORSAR and Graefenberg

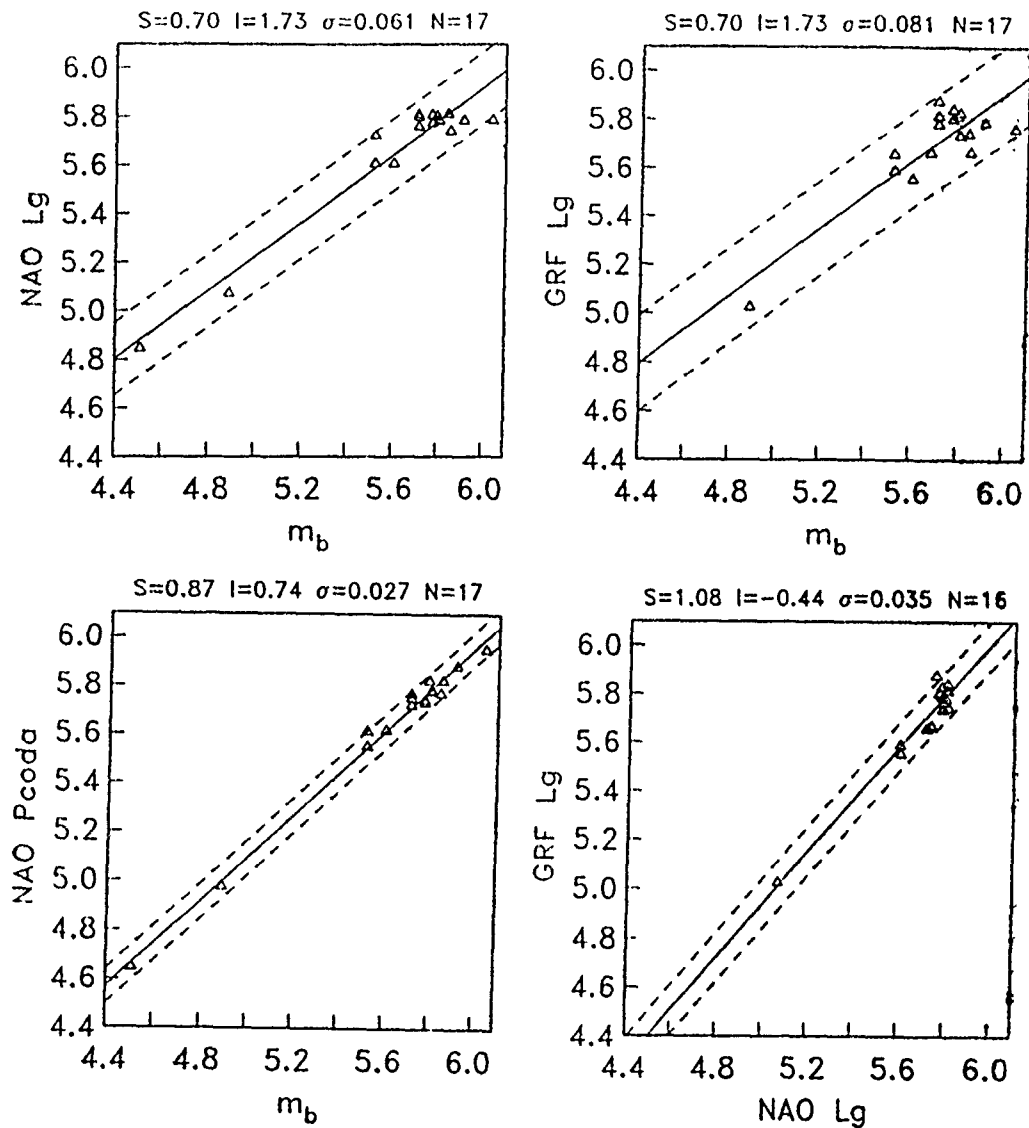


**Fig. 2.4.5.** Plots showing the correspondence between RMS Lg at NORSAR and Graefenberg and world wide  $m_b$ . Note that neither NORSAR nor GRF Lg correlates well with  $m_b$  ((a) and (b)), but they are mutually very consistent (d). Also note the excellent correspondence between  $m_b$  and NORSAR P-coda magnitude (c).



## 2.5 Summaries of Quarterly Technical Reports submitted

During FY91, three quarterly technical reports were submitted on this contract. The abstracts of these papers are given in the following.

### 2.5.1 Scattering of regional $P_n$ by Moho topography -- T. Kværna<sup>1</sup> and D.J. Doornbos<sup>2</sup> (<sup>1</sup> NTNF/NORSAR, Kjeller, Norway, and <sup>2</sup> Institute of Geophysics, University of Oslo, Norway)

The often observed relatively large amplitudes in the later part of the  $P_n$  signal cannot be explained with the traditional interpretation of  $P_n$  in 1-D crust-mantle models. To determine the cause of these characteristics, we have analyzed in some detail the NORESS array records of  $P_n$  from a suite of quarry blasts in S.W. Norway. Application of wide-band frequency-wavenumber analysis to these records confirms that there is a slowness and azimuth anomaly associated with the dominant part of the wavetrain and that it is confined to a particular frequency range. Moreover, the scattering source of the anomaly is determined to be at Moho depth, which is consistent with the concept of scattering by topographic relief. We demonstrate the viability of this concept by means of numerical experiments, showing that for realistic models of topography, the energy flux of scattered P can dominate the specular flux (i.e., the flux in the direction defined by the ray crossing a plane interface) for incidence angles approaching the critical angle of  $P_n$ . Since the effects appear to be systematic, we have the possibility to calibrate the  $P_n$  parameters for event location and velocity determination purposes.

### 2.5.2 Integrated array and 3-component processing using a "microarray" -- T. Kværna and F. Ringdal (NTNF/NORSAR, Kjeller, Norway)

A "microarray" as defined in this paper is modeled on a subgeometry of the NORESS array (Mykkeltveit et al, 1990) and comprises a 3-component center seismometer surrounded by 3 closely spaced vertical-component sensors deployed over a typical aperture of 0.3 km. Analysis of five days of continuous data has shown that such a system combines the benefits of array and 3-component processing in providing reliable automatic detection, phase identification and location of weak seismic events at local and regional distances. The data processing has comprised a) multiple-band filtering, b) coherent and incoherent beamforming, c) STA/LTA threshold detection, d) broadband frequency wavenumber (f-k) analysis and e) automatic phase association and event location. Using vertical components only, broadband f-k array analysis enables correct phase identification (P-type or S-type phase) in 95 per cent of the cases, and gives S-wave azimuths with a root-mean-square (RMS) deviation of 13.9 degrees from the estimates of the full NORESS array. It is particularly significant that the small array eliminates the need for introducing particle motion models, which creates ambiguities in 3-component analysis of secondary phases when interfering SH and SV phases occur. P-phase azimuths are estimated using integrated array and 3-component f-k analysis, and have an RMS deviation relative to NORESS of only 9.6 degrees. Compared to the full NORESS array, the P-wave detection capability is good for events with epicenters within 500 km of the station, but for greater distances the performance is significantly reduced. The S-phase detection capability is

enhanced by incoherent beamforming of the horizontal channels, and approaches that of NORESS at all distances. A considerable reduction in the detector false alarm rate is achieved by imposing constraints on the estimates of apparent velocity obtained from the f-k analysis before accepting a detected phase.

### **2.5.3 Diffraction and seismic tomography -- D.J. Doornbos (Institute of Geophysics, University of Oslo, Norway)**

Diffraction tomography is formulated in such a way that the data (travel time -- or wave-form perturbations) are related to the medium perturbations through the sum of two terms. The first term is the ray integral of ordinary tomography and involves only phase perturbations. The additional diffraction term involves both phase and amplitude perturbations. The diffraction term is linear in the gradients of the velocity perturbation in an acoustic medium, the gradients of the elastic and density perturbations in an elastic medium, and the gradients of the boundary perturbations the wave is crossing. This formulation has the additional advantage that unwanted diffractions from the nonphysical boundary of the region under study can be easily removed. Acoustic scattering, elastic scattering, and scattering by boundary perturbations are analyzed separately. Attention is paid to the adequacy of the acoustic approximation, and to the difference between perturbations of a boundary level (topography) and perturbations of boundary conditions. These differences are irrelevant for ordinary seismic tomography. All results are based on first-order approximations (Born or Rytov), as is the case for other published methods of diffraction tomography.

Prof. Thomas Ahrens  
Seismological Lab, 252-21  
Division of Geological & Planetary Sciences  
California Institute of Technology  
Pasadena, CA 91125

Prof. Keiiti Aki  
Center for Earth Sciences  
University of Southern California  
University Park  
Los Angeles, CA 90089-0741

Prof. Shelton Alexander  
Geosciences Department  
403 Deike Building  
The Pennsylvania State University  
University Park, PA 16802

Dr. Ralph Alewine, III  
DARPA/NMRO  
3701 North Fairfax Drive  
Arlington, VA 22203-1714

Prof. Charles B. Archambeau  
CIRES  
University of Colorado  
Boulder, CO 80309

Dr. Thomas C. Bache, Jr.  
Science Applications Int'l Corp.  
10260 Campus Point Drive  
San Diego, CA 92121 (2 copies)

Prof. Muawia Barazangi  
Institute for the Study of the Continent  
Cornell University  
Ithaca, NY 14853

Dr. Jeff Barker  
Department of Geological Sciences  
State University of New York  
at Binghamton  
Vestal, NY 13901

Dr. Douglas R. Baumgardt  
ENSCO, Inc  
5400 Port Royal Road  
Springfield, VA 22151-2388

Dr. Susan Beck  
Department of Geosciences  
Building #77  
University of Arizona  
Tucson, AZ 85721

Dr. T.J. Bennett  
S-CUBED  
A Division of Maxwell Laboratories  
11800 Sunrise Valley Drive, Suite 1450  
Reston, VA 22091

Dr. Robert Blandford  
AFTAC/TT, Center for Seismic Studies  
1330 North 17th Street  
Suite 1450  
Arlington, VA 22209-2308

Dr. G.A. Bollinger  
Department of Geological Sciences  
Virginia Polytechnical Institute  
21044 Derring Hall  
Blacksburg, VA 24061

Dr. Stephen Bratt  
Center for Seismic Studies  
1300 North 17th Street  
Suite 1450  
Arlington, VA 22209-2308

Dr. Lawrence Burdick  
Woodward-Clyde Consultants  
566 El Dorado Street  
Pasadena, CA 91109-3245

Dr. Robert Burrige  
Schlumberger-Doll Research Center  
Old Quarry Road  
Ridgefield, CT 06877

Dr. Jerry Carter  
Center for Seismic Studies  
1300 North 17th Street  
Suite 1450  
Arlington, VA 22209-2308

Dr. Eric Chael  
Division 9241  
Sandia Laboratory  
Albuquerque, NM 87185

Prof. Vernon F. Cormier  
Department of Geology & Geophysics  
U-45, Room 207  
University of Connecticut  
Storrs, CT 06268

Prof. Anton Dainty  
Earth Resources Laboratory  
Massachusetts Institute of Technology  
42 Carleton Street  
Cambridge, MA 02142

Prof. Steven Day  
Department of Geological Sciences  
San Diego State University  
San Diego, CA 92182

Dr. Art Frankel  
U.S. Geological Survey  
922 National Center  
Reston, VA 22092

Marvin Denny  
U.S. Department of Energy  
Office of Arms Control  
Washington, DC 20585

Dr. Cliff Frolich  
Institute of Geophysics  
8701 North Mopac  
Austin, TX 78759

Dr. Zoltan Der  
ENSCO, Inc.  
5400 Port Royal Road  
Springfield, VA 22151-2388

Dr. Holly Given  
IGPP, A-025  
Scripps Institute of Oceanography  
University of California, San Diego  
La Jolla, CA 92093

Prof. Adam Dziewonski  
Hoffman Laboratory, Harvard University  
Dept. of Earth Atmos. & Planetary Sciences  
20 Oxford Street  
Cambridge, MA 02138

Dr. Jeffrey W. Given  
SAIC  
10260 Campus Point Drive  
San Diego, CA 92121

Prof. John Ebel  
Department of Geology & Geophysics  
Boston College  
Chestnut Hill, MA 02167

Dr. Dale Glover  
Defense Intelligence Agency  
ATTN: ODT-1B  
Washington, DC 20301

Eric Fielding  
SNEE Hall  
INSTOC  
Cornell University  
Ithaca, NY 14853

Dr. Indra Gupta  
Teledyne Geotech  
314 Montgomery Street  
Alexandria, VA 22314

Dr. Mark D. Fisk  
Mission Research Corporation  
735 State Street  
P.O. Drawer 719  
Santa Barbara, CA 93102

Dan N. Hagedorn  
Pacific Northwest Laboratories  
Battelle Boulevard  
Richland, WA 99352

Prof Stanley Flate  
Applied Sciences Building  
University of California, Santa Cruz  
Santa Cruz, CA 95064

Dr. James Hannon  
Lawrence Livermore National Laboratory  
P.O. Box 808  
L-205  
Livermore, CA 94550

Dr. John Foley  
NER-Geo Sciences  
1100 Crown Colony Drive  
Quincy, MA 02169

Dr. Roger Hansen  
HQ AFTAC/TTR  
Patrick AFB, FL 32925-6001

Prof. Donald Forsyth  
Department of Geological Sciences  
Brown University  
Providence, RI 02912

Prof. David G. Harkrider  
Seismological Laboratory  
Division of Geological & Planetary Sciences  
California Institute of Technology  
Pasadena, CA 91125

Prof. Danny Harvey  
CIRES  
University of Colorado  
Boulder, CO 80309

Prof. Donald V. Helmberger  
Seismological Laboratory  
Division of Geological & Planetary Sciences  
California Institute of Technology  
Pasadena, CA 91125

Prof. Eugene Herrin  
Institute for the Study of Earth and Man  
Geophysical Laboratory  
Southern Methodist University  
Dallas, TX 75275

Prof. Robert B. Herrmann  
Department of Earth & Atmospheric Sciences  
St. Louis University  
St. Louis, MO 63156

Prof. Lane R. Johnson  
Seismographic Station  
University of California  
Berkeley, CA 94720

Prof. Thomas H. Jordan  
Department of Earth, Atmospheric &  
Planetary Sciences  
Massachusetts Institute of Technology  
Cambridge, MA 02139

Prof. Alan Kafka  
Department of Geology & Geophysics  
Boston College  
Chestnut Hill, MA 02167

Robert C. Kemerait  
ENSCO, Inc.  
445 Pineda Court  
Melbourne, FL 32940

Dr. Max Koontz  
U.S. Dept. of Energy/DP 5  
Forrestal Building  
1000 Independence Avenue  
Washington, DC 20585

Dr. Richard LaCoss  
MIT Lincoln Laboratory, M-200B  
P.O. Box 73  
Lexington, MA 02173-0073

Dr. Fred K. Lamb  
University of Illinois at Urbana-Champaign  
Department of Physics  
1110 West Green Street  
Urbana, IL 61801

Prof. Charles A. Langston  
Geosciences Department  
403 Deike Building  
The Pennsylvania State University  
University Park, PA 16802

Jim Lawson, Chief Geophysicist  
Oklahoma Geological Survey  
Oklahoma Geophysical Observatory  
P.O. Box 8  
Leonard, OK 74043-0008

Prof. Thorne Lay  
Institute of Tectonics  
Earth Science Board  
University of California, Santa Cruz  
Santa Cruz, CA 95064

Dr. William Leith  
U.S. Geological Survey  
Mail Stop 928  
Reston, VA 22092

Mr. James F. Lewkowicz  
Phillips Laboratory/GPEH  
Hanscom AFB, MA 01731-5000( 2 copies)

Mr. Alfred Lieberman  
ACDA/VI-OA State Department Building  
Room 5726  
320-21st Street, NW  
Washington, DC 20451

Prof. L. Timothy Long  
School of Geophysical Sciences  
Georgia Institute of Technology  
Atlanta, GA 30332

Dr. Robert Masse  
Denver Federal Building  
Box 25046, Mail Stop 967  
Denver, CO 80225

Dr. Randolph Martin, III  
New England Research, Inc.  
76 Olcott Drive  
White River Junction, VT 05001

Dr. Gary McCartor  
Department of Physics  
Southern Methodist University  
Dallas, TX 75275

Prof. Thomas V. McEvilly  
Seismographic Station  
University of California  
Berkeley, CA 94720

Dr. Art McGarr  
U.S. Geological Survey  
Mail Stop 977  
U.S. Geological Survey  
Menlo Park, CA 94025

Dr. Keith L. McLaughlin  
S-CUBED  
A Division of Maxwell Laboratory  
P.O. Box 1620  
La Jolla, CA 92038-1620

Stephen Miller & Dr. Alexander Florence  
SRI International  
333 Ravenswood Avenue  
Box AF 116  
Menlo Park, CA 94025-3493

Prof. Bernard Minster  
IGPP, A-025  
Scripps Institute of Oceanography  
University of California, San Diego  
La Jolla, CA 92093

Prof. Brian J. Mitchell  
Department of Earth & Atmospheric Sciences  
St. Louis University  
St. Louis, MO 63156

Mr. Jack Murphy  
S-CUBED  
A Division of Maxwell Laboratory  
11500 Sunrise Valley Drive, Suite 1212  
Reston, VA 22091 (2 Copies)

Dr. Keith K. Nakanishi  
Lawrence Livermore National Laboratory  
L-025  
P.O. Box 808  
Livermore, CA 94550

Dr. Carl Newton  
Los Alamos National Laboratory  
P.O. Box 1663  
Mail Stop C335, Group ESS-3  
Los Alamos, NM 87545

Dr. Bao Nguyen  
HQ AFTAC/TTR  
Patrick AFB, FL 32925

Prof. John A. Orcutt  
IGPP, A-025  
Scripps Institute of Oceanography  
University of California, San Diego  
La Jolla, CA 92093

Prof. Jeffrey Park  
Kline Geology Laboratory  
P.O. Box 6666  
New Haven, CT 06511-8130

Dr. Howard Patton  
Lawrence Livermore National Laboratory  
L-025  
P.O. Box 808  
Livermore, CA 94550

Dr. Frank Pilotte  
HQ AFTAC/TT  
Patrick AFB, FL 32925-6001

Dr. Ray J. Pulli  
Radix Systems, Inc.  
2 Taft Court, Suite 203  
Rockville, MD 20850

Dr. Robert Reinke  
ATTN: FCTVID  
Field Command  
Defense Nuclear Agency  
Kirtland AFB, NM 87115

Prof. Paul G. Richards  
Lamont-Doherty Geological Observatory  
of Columbia University  
Palisades, NY 10964

Mr. Wilmer Rivers  
Teledyne Geotech  
314 Montgomery Street  
Alexandria, VA 22314

Dr. George Rothe  
HQ AFTAC/ITR  
Patrick AFB, FL 32925-6001

Dr. Alan S. Ryall, Jr.  
DARPA/NMRO  
3701 North Fairfax Drive  
Arlington, VA 22209-1714

Dr. Richard Sailor  
TASC, Inc.  
55 Walkers Brook Drive  
Reading, MA 01867

Prof. Charles G. Sammis  
Center for Earth Sciences  
University of Southern California  
University Park  
Los Angeles, CA 90089-0741

Prof. Christopher H. Scholz  
Lamont-Doherty Geological Observatory  
of Columbia University  
Palisades, CA 10964

Dr. Susan Schwartz  
Institute of Tectonics  
1156 High Street  
Santa Cruz, CA 95064

Secretary of the Air Force  
(SAFRD)  
Washington, DC 20330

Office of the Secretary of Defense  
DDR&E  
Washington, DC 20330

Thomas J. Sereno, Jr.  
Science Application Int'l Corp.  
10260 Campus Point Drive  
San Diego, CA 92121

Dr. Michael Shore  
Defense Nuclear Agency/SPSS  
6801 Telegraph Road  
Alexandria, VA 22310

Dr. Matthew Sibol  
Virginia Tech  
Seismological Observatory  
4044 Derring Hall  
Blacksburg, VA 24061-0420

Prof. David G. Simpson  
IRIS, Inc.  
1616 North Fort Myer Drive  
Suite 1400  
Arlington, VA 22209

Donald L. Springer  
Lawrence Livermore National Laboratory  
L-025  
P.O. Box 808  
Livermore, CA 94550

Dr. Jeffrey Stevens  
S-CUBED  
A Division of Maxwell Laboratory  
P.O. Box 1620  
La Jolla, CA 92038-1620

Lt. Col. Jim Stobie  
ATTN: AFOSR/NL  
Bolling AFB  
Washington, DC 20332-6448

Prof. Brian Stump  
Institute for the Study of Earth & Man  
Geophysical Laboratory  
Southern Methodist University  
Dallas, TX 75275

Prof. Jeremiah Sullivan  
University of Illinois at Urbana-Champaign  
Department of Physics  
1110 West Green Street  
Urbana, IL 61801

Prof. L. Sykes  
Lamont-Doherty Geological Observatory  
of Columbia University  
Palisades, NY 10964

Dr. David Taylor  
ENSCO, Inc.  
445 Pineda Court  
Melbourne, FL 32940

Dr. Steven R. Taylor  
Los Alamos National Laboratory  
P.O. Box 1663  
Mail Stop C335  
Los Alamos, NM 87545

Prof. Clifford Thurber  
University of Wisconsin-Madison  
Department of Geology & Geophysics  
1215 West Dayton Street  
Madison, WI 53706

Prof. M. Nafi Toksoz  
Earth Resources Lab  
Massachusetts Institute of Technology  
42 Carleton Street  
Cambridge, MA 02142

Dr. Larry Turnbull  
CIA-OSWR/NED  
Washington, DC 20505

Dr. Gregory van der Vink  
IRIS, Inc.  
16116 North Fort Myer Drive  
Suite 1440  
Arlington, VA 22209

Dr. Karl Veith  
EG&G  
5211 Auth Road  
Suite 240  
Suitland, MD 20746

Prof. Terry C. Wallace  
Department of Geosciences  
Building #77  
University of Arizona  
Tucson, AZ 85721

Dr. Thomas Weaver  
Los Alamos National Laboratory  
P.O. Box 1663  
Mail Stop C335  
Los Alamos, NM 87545

Dr. William Wortman  
Mission Research Corporation  
8560 Cinderbed Road  
Suite 700  
Newington, VA 22122

Prof. Francis T. Wu  
Department of Geological Sciences  
State University of New York  
at Binghamton  
Vestal, NY 13901

AFTAC/CA  
(STINFO)  
Patrick AFB, FL 32925-6001

DARPA/PM  
3701 North Fairfax Drive  
Arlington, VA 22203-1714

DARPA/RMO/RETRIEVAL  
3701 North Fairfax Drive  
Arlington, VA 22203-1714

DARPA/RMO/SECURITY OFFICE  
3701 North Fairfax Drive  
Arlington, VA 2203-1714

HQ DNA  
ATTN: Technical Library  
Washington, DC 20305

Defense Intelligence Agency  
Directorate for Scientific & Technical Intelligence  
ATTN: DTIB  
Washington, DC 20340-6158

Defense Technical Information Center  
Cameron Station  
Alexandria, VA 22314 (2 Copies)

TACTEC  
Battelle Memorial Institute  
505 King Avenue  
Columbus, OH 43201 (Final Report)

Phillips Laboratory  
ATTN: XPG  
Hanscom AFB, MA 01731-5000

Phillips Laboratory  
ATTN: GPE  
Hanscom AFB, MA 01731-5000

Phillips Laboratory  
ATTN: TSML  
Hanscom AFB, MA 01731-5000

Phillips Laboratory  
ATTN: SUL  
Kirtland, NM 87117 (2 copies)



Dr. Michel Bouchon  
I.R.I.G.M.-B.P. 68  
38402 St. Martin D'Heres  
Cedex, FRANCE

Prof. Keith Priestley  
University of Cambridge  
Bullard Labs, Dept. of Earth Sciences  
Madingley Rise, Madingley Road  
Cambridge CB3 0EZ, ENGLAND

Dr. Michel Campillo  
Observatoire de Grenoble  
I.R.I.G.M.-B.P. 53  
38041 Grenoble, FRANCE

Dr. Jorg Schlittenhardt  
Federal Institute for Geosciences & Nat'l Res.  
Postfach 510153  
D-3000 Hannover 51, GERMANY

Dr. Kin Yip Chun  
Geophysics Division  
Physics Department  
University of Toronto  
Ontario, CANADA

Dr. Johannes Schweitzer  
Institute of Geophysics  
Ruhr University/Bochum  
P.O. Box 1102148  
4360 Bochum 1, GERMANY

Prof. Hans-Peter Harjes  
Institute for Geophysics  
Ruhr University/Bochum  
P.O. Box 102148  
4630 Bochum 1, GERMANY

Prof. Eystein Husebye  
NTNF/NORSAR  
P.O. Box 51  
N-2007 Kjeller, NORWAY

David Jepsen  
Acting Head, Nuclear Monitoring Section  
Bureau of Mineral Resources  
Geology and Geophysics  
G.P.O. Box 378, Canberra, AUSTRALIA

Ms. Eva Johannisson  
Senior Research Officer  
National Defense Research Inst.  
P.O. Box 27322  
S-102 54 Stockholm, SWEDEN

Dr. Peter Marshall  
Procurement Executive  
Ministry of Defense  
Blacknest, Brimpton  
Reading FG7-FRS, UNITED KINGDOM

Dr. Bernard Massinon, Dr. Pierre Mèchler  
Societe Radiomana  
27 rue Claude Bernard  
75005 Paris, FRANCE (2 Copies)

Dr. Svein Mykkeltveit  
NTNF/NORSAR  
P.O. Box 51  
N-2007 Kjeller, NORWAY (3 Copies)